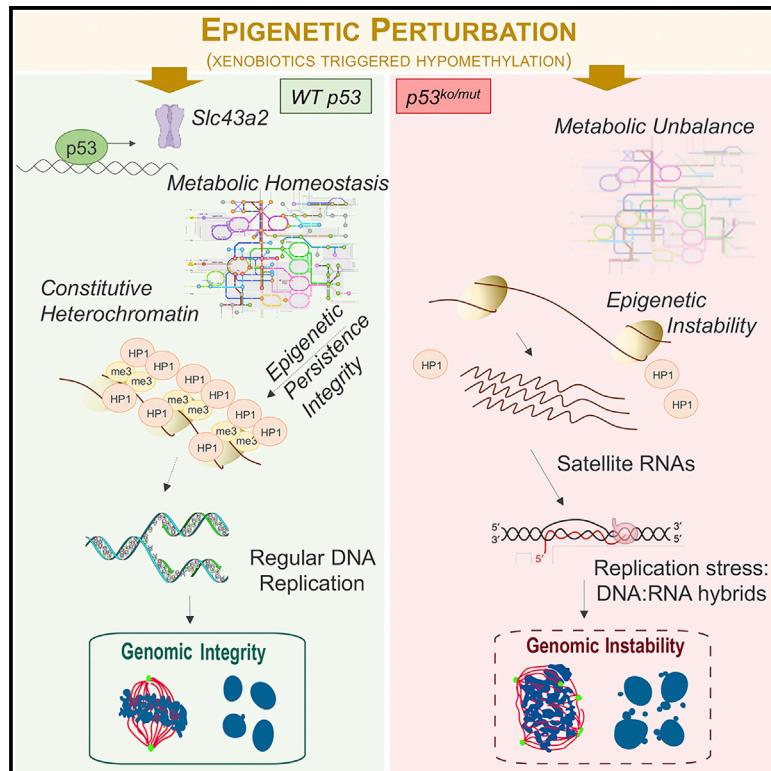# Metabolic regulation by p53 prevents R-loop-associated genomic instability

Graphical abstract

Authors

Emanuele Panatta, Alessio Butera, Eleonora Mammarella, ..., Richard A. Knight, Gerry Melino, Ivano Amelio

Correspondence

ivano.amelio@uni-konstanz.de

In brief

Panatta et al. demonstrate that cells lacking functional p53 when exposed to stress undergo genomic instability as a consequence of inability to preserve the constitutive heterochromatin status. p53 ensures adequate level of S-adenosylmethionine, which instates persistence of histone methylation and prevents loss of genomic integrity.

Highlights

- p53 inactivation reduces the level of S-adenosylmethionine (SAM)

- p53 preserves stressed constitutive heterochromatin

- p53 prevents aberrant satellite transcription and R-loop-dependent genomic instability

- Restoration of SAM reinstates genomic integrity in p53 deficiency

Cell Reports

Article

Metabolic regulation by p53 prevents R-loop-associated genomic instability

Emanuele Panatta,[1] Alessio Butera,[1,2] Eleonora Mammarella,[1] Consuelo Pitolli,[1] Alessandro Mauriello,[1] Marcel Leist,[3] Richard A. Knight,[1] Gerry Melino,[1] and Ivano Amelio[1,2,4,*]

[1]Department of Experimental Medicine, TOR, University of Rome Tor Vergata, 00133 Rome, Italy
[2]Division for Systems Toxicology, Department of Biology, University of Konstanz, Konstanz, Germany
[3]Division for *In Vitro* Toxicology and Biomedicine, Department of Biology, University of Konstanz, Konstanz, Germany
[4]Lead contact
*Correspondence: ivano.amelio@uni-konstanz.de
https://doi.org/10.1016/j.celrep.2022.111568

SUMMARY

Gene-environment interactions can perturb the epigenome, triggering network alterations that participate in cancer pathogenesis. Integrating epigenomics, transcriptomics, and metabolic analyses with functional perturbation, we show that the tumor suppressor p53 preserves genomic integrity by empowering adequate levels of the universal methyl donor S-adenosylmethionine (SAM). In p53-deficient cells, perturbation of DNA methylation promotes derepression of heterochromatin, massive loss of histone H3-lysine 9 methylation, and consequent upregulation of satellite RNAs that triggers R-loop-associated replication stress and chromosomal aberrations. In p53-deficient cells, the inadequate SAM level underlies the inability to respond to perturbation because exogenous reintroduction of SAM represses satellite elements and restores the ability to cope with stress. Mechanistically, p53 transcriptionally controls genes involved in one-carbon metabolism, including Slc43a2, the methionine uptake transporter that is critical for SAM synthesis. Supported by clinical data, our findings shed light on the role of p53-mediated metabolism in preventing unscheduled R-loop-associated genomic instability.

INTRODUCTION

Metabolic control of chromatin dynamics is essential for the development and integrity of somatic tissues (Dai et al., 2020; Haws et al., 2020a). Functional interactions between the microenvironment (metabolites and oxygen fluctuations), xenobiotics (toxic injury), and genetics can trigger global alteration in DNA methylation and histone posttranslational modifications, referred to hereafter as epigenetic, with consequences for gene expression and genomic integrity (Alonso-Curbelo et al., 2021; Janssen et al., 2018). Genome-wide loss of methylation of DNA and histone (i.e., epigenetic) is generally associated with genomic instability and is observed in aging and cancer development (Wilson et al., 2007). Epigenetic methylations are influenced by the methionine cycle, which provides the universal methyl donor S-adenosylmethionine (SAM). Altered SAM abundance is directly sensitized by chromatin states, and adaptive mechanisms are in place to counterbalance methyl donor depletion (Mentch et al., 2015). Within these, dynamic control of methylation of H3 lysine 9 (H3K9me) is essential to preserve silent constitutive heterochromatin (Haws et al., 2020b). Constitutive heterochromatin is a major component of the eukaryotic genome and is typically situated at pericentromeric and telomeric regions; it includes repetitive satellite DNA and mobile elements such as retrotransposons. Perturbation of the fine epigenetic homeostasis of constitutive heterochromatin can have far-reaching

consequences for genome integrity and tumorigenesis (Janssen et al., 2018). Loss of heterochromatin is often observed in cancer, and alterations of the mechanisms controlling repressive H3K9me result in aneuploidy, mitotic defects, and chromosomal abnormalities (Methot et al., 2021; Zeller et al., 2016). Upon SAM depletion, epigenetic persistence is instated by preferential monomethylation of histone H3 lysine 9 (H3K9me1), which compensates for the loss of trimethylation (H3K9me3), ensuring the stability of heterochromatin and preserving residual repressive H3K9me (Haws et al., 2020b). Metabolic control of H3K9me is therefore essential to ensure epigenetic persistence upon stress, and failure to implement these mechanisms leads to severe irreversible damage.

The tumor suppressor p53 is the most frequently mutated gene across all human cancers (Kastenhuber and Lowe, 2017; Laptenko and Prives, 2017). Although implicated in cancer metabolism and genomic integrity via multiple mechanisms, the molecular basis underlying p53-dependent maintenance of genome integrity appears to be fundamentally complex (Aubrey et al., 2018; Brady et al., 2011; Kruiswijk et al., 2015; Valente et al., 2013). Here, we propose crosstalk between p53-driven metabolism and epigenetic control of constitutive heterochromatin as the basis for p53-mediated genomic integrity. Using pancreatic cancer as a model, we show that p53 deficiency leads to a reduction in the universal methyl donor SAM, leaving the cells deprived of defense against epigenetic perturbations. Perturbed
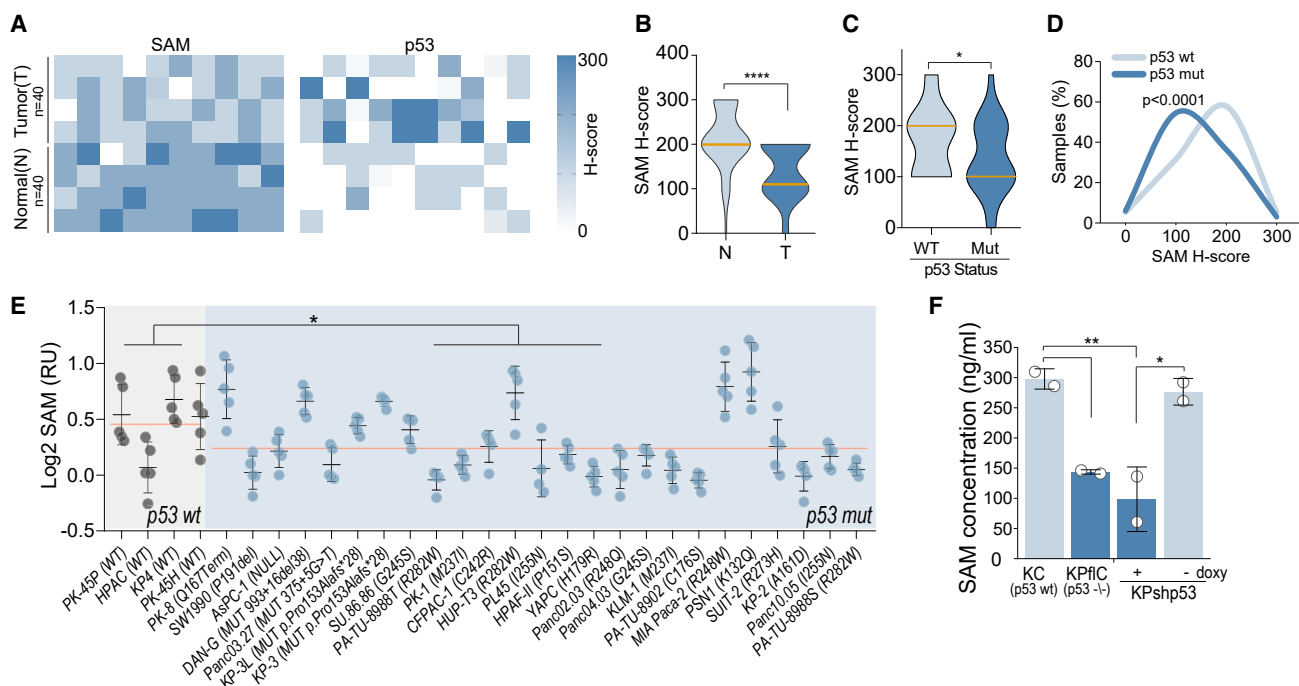
Figure 1. Inactivation of p53 leads to a reduction in SAM level in PDAC

(A) Heatmap showing the H score of SAM and p53 from PDAC tissue microarray analysis.

(B) SAM H score in normal (N, n = 52) and tumor (T, n = 52) pancreatic tissue. The orange line indicates the median of the distributions. ****p < 0.0001. The p values were calculated by unpaired and nonparametric Mann-Whitney test (two tailed).

(C and D) Distribution of SAM levels (H score) in p53 WT and p53-mutant tissues. *p < 0.05. The p values in (C) were calculated by unpaired and nonparametric Mann-Whitney test (two tailed). The p values in (D) were calculated by ordinary chi-square test with 3° of freedom.

(E) Intracellular SAM level in *TP53* WT versus *TP53* mutant human pancreatic cancer cell lines; n = 5 biological replicates per cell line. Average intracellular SAM level is indicated by the light red line. *p < 0.05. The p values were calculated with ordinary one-way ANOVA with Tukey's correction. Source: (Daemen et al. 2015).

(F) Intracellular SAM concentration in murine *Trp53* WT (KC and KP − doxy) versus *Trp53⁻/⁻* (KPᶠˡC and KP + doxy) PDAC cell lines. *p < 0.05, **p < 0.01. The p values were calculated by ordinary one-way ANOVA with Dunnett's correction; n = 2 biological replicates (white dots). Data are presented as mean ± SEM.
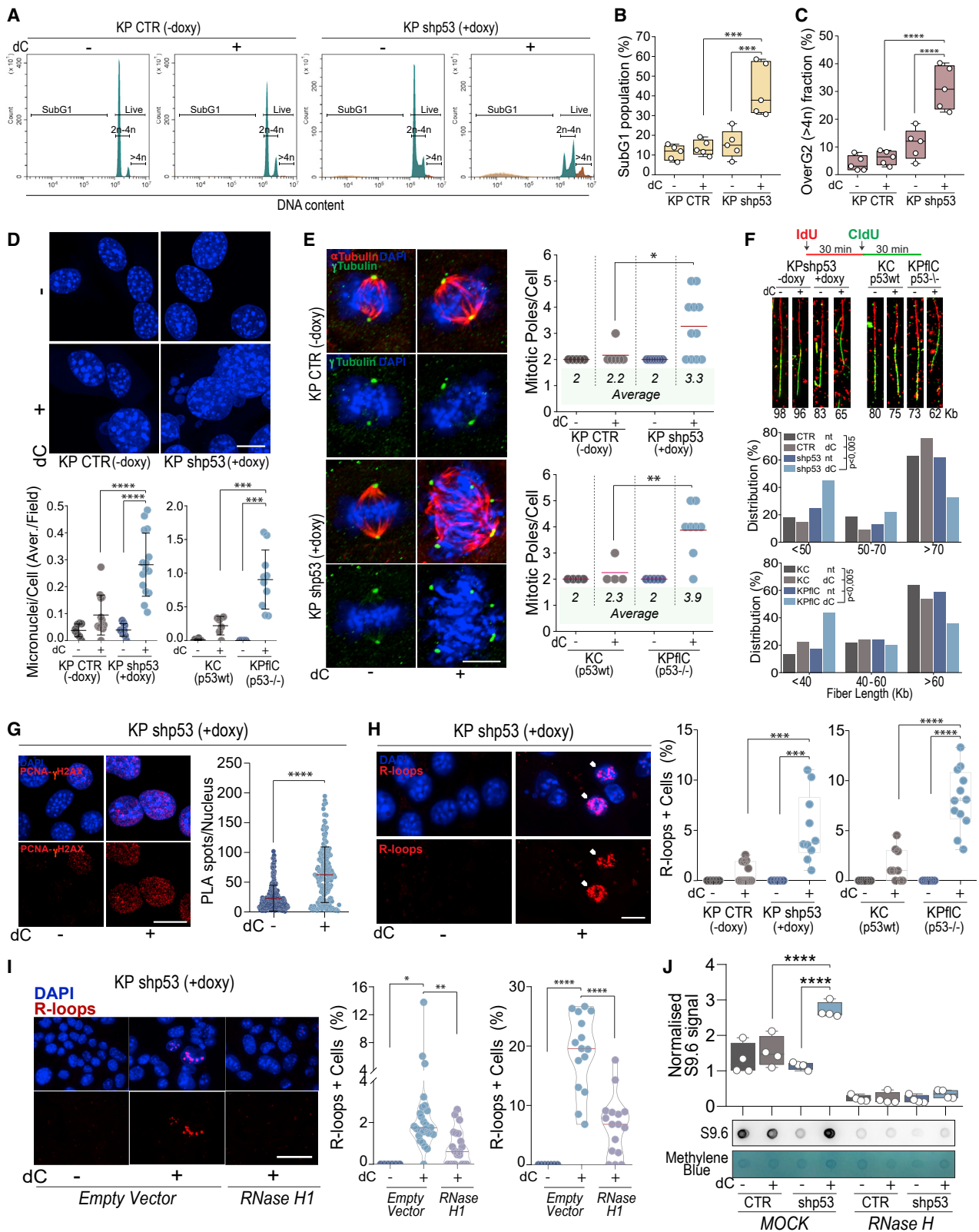
p53-deficient cells undergo accumulation of unscheduled R loops, replication stress, and chromosome breakage, leading to genomic instability. R loops originate from massive upregulation of pericentric tandem-repeat transcripts caused by epigenetic instability of constitutive heterochromatin because of inability to preserve H3K9me. Silencing of pericentric tandem-repeat transcripts or excision of unscheduled R loops reinstates genome integrity. Mechanistically, p53 controls expression of genes that influence the methyl donor SAM, including *Slc43a2*, the transporter for methionine uptake. Thus, cells lacking p53 are metabolically inadequate to preserve global epigenetic integrity upon perturbation, undergoing epigenetic instability of constitutive heterochromatin. Exogenous SAM administration preserves genome integrity even in the absence of p53. Supported by clinical evidence, we propose that metabolic inadequacy is the basis of p53-associated genomic instability.

RESULTS

p53 inactivation correlates with reduced SAM in human pancreatic ductal adenocarcinoma (PDAC)

Oncogenic deregulation has long been associated with metabolic rewiring in cancer (Hirschey et al., 2015). Although the uni-

versal methyl donor for DNA and histone methylation, SAM, is acknowledged to represent a critical hub in the metabolism-epigenome interaction, it is unclear whether and how its deregulation participates in cancer pathogenesis. Conducting an immunohistochemistry analysis on a tissue microarray of matched tumor samples of PDAC and normal adjacent tissue, we identified a general reduction in SAM levels in the process of transformation (Figures 1A, 1B, and S1A–S1C). We also revealed that SAM abundance was negatively correlated with p53 mutations in cancer lesions (Figures 1A, 1C, 1D, and S1D). The average SAM level of human pancreatic cancer cell lines carrying p53 inactivating mutations was lower than the average of p53 wild-type (WT) cell lines (Figure 1E). To determine a causative link between p53 and SAM levels, we employed a model system that allowed controlled loss and re-introduction of p53 in an otherwise similar genetic background; this was represented by a panel of mouse PDAC cells derived from tumors that arose in mice carrying pancreas-specific expression of oncogenic Kras (*LSL-KRAS^G12D*) and WT *Trp53* (KC cells), deletion of *Trp53* (KP^fl^C cells, *p53⁻/⁻*), loss of p53 via doxycycline-inducible short hairpin RNA (shRNA) targeting *Trp53* (KPshp53 cells) (Morris et al., 2019), or a mutated form of p53 with substitution of arginine with a histidine in codon 270 (KPC270, p53^R270H) (Figures S1E

and S1F). Levels of SAM were lower in KP^flC and KPshp53 cells than in KC cells, but the SAM levels fully recovered upon withdrawal of doxycycline in KPshp53 cells (i.e., reintroduction of p53) (Figure 1F). Thus, inactivation of p53 in PDAC leads to a reduced abundance of SAM.

Epigenetic perturbation triggers R-loop-associated genomic instability in p53-deficient cells

An adequate level of SAM is essential for DNA and histone methylation (Mentch et al., 2015), allowing active response to perturbation and recovery of their functional epigenomes (Sanderson et al., 2019). Exposure to (micro)environmental stressors, including nutritional status, oxygen fluctuation, xenobiotics (tobacco smoke, alcohol, air pollution, etc.), and senescence affects global and site-specific DNA methylation (Martin and Fry, 2018). Thus, we reasoned that, because of the alteration in SAM levels, p53 inactivation determines a weakness in cells exposed to perturbation of epigenetic methylation. One of the best-established exogenous epigenetic modifications is drug-induced DNA hypomethylation by decitabine (dC). This affects chromatin conformation and models various microenvironmental stressors. Under such conditions, cells may require adequate SAM levels/p53 status to maintain their chromatin homeostasis. To test this hypothesis, we analyzed the response of mouse cells derived from Kras-driven PDAC (Figures S1E and S1F) to perturbation of DNA methylation by dC, hereafter referred to as epigenetic perturbation. Analysis of DNA content by propidium iodide staining followed by flow cytometry analysis showed that perturbed p53-proficient cells do not display any major sub-G1 population (cell death; Figures 2A and 2B) or alteration of the distribution of cell cycle phases (Figure S2A). In contrast, p53-deficient cells displayed a heterogeneous response, with a subpopulation of cells undergoing cell death

(sub-G1; Figures 2A and 2B) and a subpopulation displaying features of aneuploidy (DNA content > 4 n, Figure 2C), not observed in p53-proficient cells. Analyses of micronuclei and mitotic poles indicated occurrence of chromosomal aberrations and mitotic segregation errors (Figures 2D, 2E, and S2B–S2D), confirming that epigenetic perturbation triggers hallmarks of large-scale genomic instability in p53-deficient cells.

We next sought a putative cause for the observed chromosomal abnormalities. Replication stress can result in structural and numerical chromosomal abnormalities (Kawabata et al., 2011); hence, we performed a DNA fiber assay in perturbed p53-proficient and p53-deficient cells. Epigenetic perturbation reduced replication fork progression and increased fork stalling in p53-deficient but not p53-proficient cells (Figures 2F, S2E, and S2F). Colocalization of γH2AX with PCNA indicated that replication stress was associated with DNA double-strand breaks (Figure 2G), accounting for chromosomal fragmentation.

Replication stress-associated DNA breaks often arise from the accumulation of unscheduled R-loops that pose an obstacle to fork progression, generating replication-transcription conflicts (Garcia-Muse and Aguilera, 2019). Hence, we tested whether R loops selectively accumulated in perturbed p53-deficient cells. Immunofluorescence analysis of R loops with the S9.6 anti-DNA:RNA hybrid monoclonal antibody revealed a significant accumulation of R-loop-positive nuclei in p53-deficient cells subjected to epigenetic perturbation (Figures 2H and S2G–S2J). The S9.6 signal was suppressed by overexpression of RNAseH1, confirming the specificity of the S9.6 antibody for DNA:RNA hybrids (Figure 2I). To strengthen the data, we analyzed the S9.6 signal by dot blot assay, confirming the selective accumulation of R loops in perturbed p53-deficient cells (Figure 2J). Unscheduled R loops are a threat to genome integrity, and our data implicate them in the

---

Figure 2. p53-deficient cells are permissive for R-loop-associated genomic instability

(A) Histogram profiles of DNA content measured by propidium iodide fluorescence-activated cell sorting (FACS) analysis in KP Control (CTR) (−doxy) and KP shp53 (+doxy) cells treated with decitabine (dC) or left untreated. A representative experiment of five independent biological replicates is shown.

(B and C) DNA content quantification (propidium iodide FACS analysis) for profiling of cell cycle phases (A), sub-G1 cells (cell death analysis, B) and more than 4 n (aneuploid) cells (aneuploidy analysis, C). n = 5 biological replicates (white dots). ***p < 0.001, ****p < 0.0001. The p values were calculated by ordinary one-way ANOVA with Tukey's correction.

(D) Micronucleus count by DAPI staining on KP CTR (−doxy), KP shp53 (+doxy), and KC (p53 WT), KPflC (p53^−/−) cells treated with dC or left untreated. Top: representative images of KP CTR (−doxy) and KP shp53 (+doxy) cells treated with dC or left untreated. Scale bar, 20 μm. Dot plots show micronuclear quantification (count per cell); each dot represents a field. ***p < 0.001, ****p < 0.0001. The p values were calculated by ordinary one-way ANOVA with Tukey's correction; data are presented as mean ±SEM.

(E) Mitotic pole analysis. Left panel: representative images of α-tubulin (red) and γ-tubulin (green) staining on KP CTR (−doxy) and KP shp53 (+doxy) cells treated with dC or left untreated. Scale bar, 5 μm. DAPI counterstains DNA. Right panels: dot plots displaying quantification of mitotic poles; each dot represents a mitotic cell. Red lines indicate average. *p < 0.05, **p < 0.01. The p values were calculated by ordinary one-way ANOVA with Tukey's correction.

(F) DNA fiber assay. Cells were exposed for 30 min to ldU (red), followed by 30 min of CldU (green). Top panel: representative fibers. Bottom panels: fiber length distribution. The p values were calculated with ordinary chi-square test with 2° of freedom.

(G) Proximity ligation assay (PLA; red) for PCNA and γH2AX on KP shp53 (+doxy) cells treated with dC or left untreated. Left panel: representative staining (PLA in red and DAPI counterstained DNA). Scale bar, 20 μm. Right panel: dot plot representing quantification of PLA-positive spots per nucleus; each dot represents a cell. Red lines indicate the average; 150–200 cells were analyzed, and data were normalized to nuclear size. ****p < 0.0001. The p values were calculated by 2-tailed unpaired t test; data are presented as mean ± SEM.

(H and I) R loop analysis of dC-treated or untreated KP CTR (−doxy), KP shp53 (+doxy), KC (p53 WT), and KPflC (p53^−/−) cells and after overexpression of RNAseH1. Also shown are representative immunofluorescence confocal images (by S9.6 antibody [Ab], red); DAPI counterstains DNA. Scale bars, 5 μm (H) and 20 μm (I). Right panels: dot plots report R-loop-positive cells per field; each dot represents a field. *p < 0.05, **p < 0.01, ***p < 0.001, ****p < 0.0001. The p values were calculated by ordinary one-way ANOVA with Tukey's correction.

(J) Dot blot analysis of S9.6 (R loop signal) of dC-treated/untreated KP CTR (−doxy) and KP shp53 (+doxy) cells with and without RNAseH1 treatment. Methylene blue was a loading control. Histograms report densitometry quantification of 4 independent biological replicates (white dots). The p values were calculated by ordinary one-way ANOVA with Tukey's correction. ****p < 0.0001.
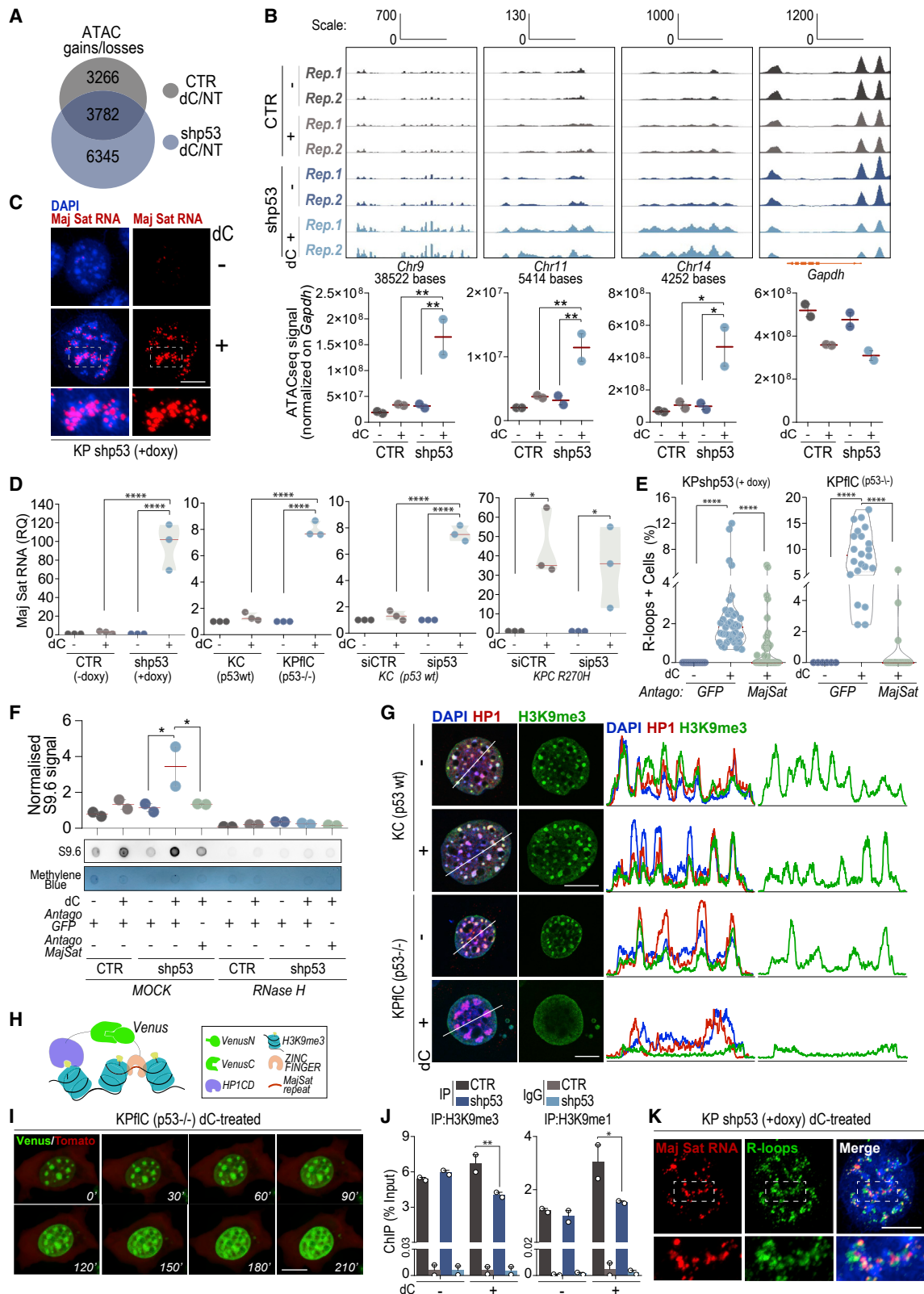
(legend on next page)

genomic instability associated with p53 loss. These findings on epigenetic perturbation as driver of unscheduled R loop formation and chromosomal abnormalities in the absence of p53 provide a possible additional mechanism for earlier observations that mutations in p53 are permissive but not causative of genomic instability (Bunz et al., 2002).

p53-depleted cells fail to implement epigenetic persistence of constitutive heterochromatin

To gain insight into the molecular causes of this genomic instability, we tracked the upstream chromatin deregulations produced by the cooperation of p53 inactivation and perturbation of DNA methylation. To this end, we performed differential genome-wide accessibility profiling (assay for transposase-accessible chromatin using sequencing [ATAC-seq]), which provides information on open chromatin region (peak) changes, referred to as ATAC gain and loss. Comparison of the effects of epigenetic perturbation on p53-proficient and p53-deficient cells indicated clearly distinct patterns of chromatin accessibility (Figures 3A, S3A, and S3B). By querying the list of ATAC changes selectively associated with perturbed p53-deficient cells, we identified a significant proportion of genomic loci containing noncoding DNA repetitive elements typically included in constitutive heterochromatin regions, particularly major satellite repeats (Figures 3B, S3C, and S3D). 85% of the repetitive sequence regions annotated in the mouse genome displayed a selective gain of chromatin accessibility in perturbed p53-deficient cells (Table S1). Analysis of the RNA level of major satellite repeats by fluorescence *in situ* hybridization (FISH) and RT-qPCR revealed an important upregulation of these satellite transcripts in perturbed p53-deficient cells (Figures 3C, 3D, and S3E–S3G), indicating that increased chromatin accessibility was associated with transcription. Upregulation of constitutive heterochromatin noncoding satellite RNAs has been linked to genomic instability in cancer (Yang et al., 2018; Zhu et al., 2011), including PDAC (Ting et al., 2011). Because a major mechanism of satellite RNA-dependent genomic instability is the accumulation of un-

scheduled R loops (Janssen et al., 2018), we asked whether a high level of major satellite RNAs was responsible for R loop accumulation in perturbed p53-deficient cells, as described in Figure 2. Confocal imaging and a dot blot assay indicated that silencing of major satellite RNAs by transfection of antisense LNA (Antago-major satellite [MajSat]) significantly reduced R loop induction (Figures 3E, 3F, S3H, and S3I). Thus, a causative link emerged between alteration of the silencing of constitutive heterochromatin noncoding satellite RNAs and unscheduled R loops in perturbed p53-deficient cells.

Upon methylation stress, the chromatin response is mediated by dynamic control of H3K9 methylation (Haws et al., 2020b). When epigenetic persistence fails, heterochromatin stability is lost, and derepression of constitutively silenced DNA elements may occur. This may lead to deleterious irreversible consequences (Haws et al., 2020b). Based on the ATAC-seq analysis, we reasoned that p53-deficient cells lose epigenetic control of their constitutive heterochromatin as a consequence of epigenetic perturbation. Mouse cells display highly condensed regions of pericentromeric heterochromatin, including repetitive MajSat DNA (chromocenters), which can be visualized by staining for heterochromatin protein (HP1), H3K9me3, or 4′,6-diamidino-2-phenylindole (DAPI) staining (Jagannathan et al., 2018). Imaging chromocenters by confocal microscopy indicated that epigenetic perturbation did not significantly affect their condensation and structure in p53-proficient cells (Figure 3G). In contrast, perturbed p53-deficient cells displayed massive diffusion of H3K9me3 signals and significant relaxation via residual HP1 and DAPI staining (Figures 3G and S3J). Consistent with heterochromatin relaxation, the nuclei of perturbed p53-deficient cells appeared enlarged (Figure S3K). To prove that epigenetic instability was associated with decondensed MajSat-containing heterochromatin, we employed modular fluorescence complementation sensors for live-cell detection of H3K9me3 signals specifically at the MajSat genomic site (Lungu et al., 2017; Figure 3H). Time-lapse analyses of p53-deficient cells exposed to dC detected very fast loss in the MajSat H3K9me3 signal between 180 and 240 min of analysis

Figure 3. p53-deficient cells are unable to preserve the stability of silent heterochromatin

(A) Venn diagram of ATAC-seq gains/losses in KP CTR (−doxy) and KP shp53 (+doxy) cells treated with dC or left untreated.

(B) Representative images of ATAC-seq tracks of heterochromatin-containing MajSat regions on chromosomes 9, 11, and 14. *Gapdh* is displayed as a reference control. Rep.1 and Rep.2 are two biological replicates. Bottom panels: quantification of ATAC-seq peaks shown in the top panels. *p < 0.05, **p < 0.01. The p values were calculated by ordinary one-way ANOVA with Fisher's LSD test. Data are presented as mean ±SEM.

(C) RNA FISH staining using a probe against the MajSat transcript (red); DAPI counterstains DNA. Scale bar, 10 μm. A representative cell per sample is shown.

(D) qRT-PCR of the major satellite (MajSat) transcript. ****p < 0.0001. The p values were calculated by RM one-way ANOVA with Fisher's LSD test; n = 3 biological replicates (dots).

(E and F) R loop quantification as a percentage of positive cells by confocal imaging (S9.6-positive cells) (E) and dot blot signal of S9.6 (F) after transfection with MajSat antisense LNA (Antago-MajSat) or antisense GFP control (Antago-GFP). In (E), each dot represents a field. ****p < 0.0001. The p values were calculated by ordinary one-way ANOVA with Tukey's correction. In (F), each dot represents an independent biological replicate. *p < 0.05. The p values were calculated by ordinary one-way ANOVA with Tukey's correction.

(G) H3K9me3 (green) and HP1 (red) immunofluorescence analysis. Left panel: representative images; scale bar, 5 μm. Right panel: histograms representing the fluorescence intensity traced following the white line in the corresponding picture of H3K9me3 (green), HP1 (red), and DAPI staining.

(H) Schematic of the BiAD Venus-based sensor. The HP1 chromodomain (*HP1CD*) binds trimethylated lysine 9 on histone 3 (H3K9me3), and the zinc-finger domain binds MajSat DNA repeats. Close proximity of the two Venus subunits (C-terminal, *VenusC*; N-terminal, *VenusN*) gives rise to a fluorescent signal.

(I) Live-cell imaging confocal analysis of KPflC (*p53⁻/⁻*) cells expressing the BiAD Venus-based sensor (green signal) to detect H3K9me3 at mouse MajSat repeats (Lungu et al., 2017). Images were scanned every 30 min starting 48 h after dC treatment (point 0); tomato fluorophore (red) was used as a viable control. Scale bar, 10 μm.

(J) ChIP-qPCR analysis of H3K9me3 and H3K9me1 in KP CTR (−doxy) and KP shp53 (+doxy) cells treated with dC or left untreated. *p < 0.05, **p < 0.001. The p value were calculated by ordinary one-way ANOVA with Tukey's correction; n = 2 biological replicates (white dots). Data are presented as mean ± SEM.

(K) MajSat RNA FISH (red) and R loop immunofluorescence (IF) (S9.6 Ab, green); DAPI counterstains DNA. Scale bar, 10 μm. A representative cell is shown.

(Figures 3I and S3L). Chromatin immunoprecipitation (ChIP) followed by qPCR detected reduced levels of H3K9me3 in perturbed p53-deficient cells. Such cells failed to accumulate compensatory H3K9me1 (Figures 3J and S3M), indicating that the mechanism of epigenetic persistence involving compensatory mono-methylation in support of loss of tri-methylation (Haws et al., 2020b) was not functioning effectively. Hence, overall, our data indicate altered dynamics of H3K9me at MajSat-containing heterochromatin in the response of p53-deficient cells to perturbation of DNA methylation. Bisulfite-converted PCR analysis indicated that DNA demethylation was equally affected in p53-proficient and p53-deficient cells, confirming that the aberrant epigenetic and transcriptional pattern was ascribed to histone methylation (Figure S3N).

Consistent with the data indicating constitutive heterochromatin deregulation as a source of R loops, we detected localization of R loops in nuclear areas compatible with heterochromatin DAPI staining by high-resolution confocal microscopy (Figures S4A–S4D). R-loop-positive cells highly overlapped with MajSat RNA-expressing cells (Figures 3K and S4E–S4H). The observed phenotype, including relaxation of constitutive heterochromatin, upregulation of MajSat RNAs, R loops, and micronuclei accumulation, was recapitulated in model systems different from Kras-driven pancreatic cancer, such as immortalized mouse fibroblasts, the NIH3T3 cell line, and immortalized mouse myoblasts (C2C12 cells) (Figures S4I–S4M). Thus, the sensitivity to epigenetic perturbation is closely related to p53 functionality rather than additional co-occurring oncogenic mutations.

Control of satellite repression is mediated by concerted cooperation of DNA and H3K9me, and dysregulation of these epigenetic marks is linked to carcinogenesis (Bailey et al., 2000; Ting et al., 2011). In response to stress-induced alterations in the equilibrium of these epigenetic marks, p53-deficient cells fail to promote epigenetic persistence, triggering a cascade of events involving upregulation of satellite RNAs, accumulation of R loops, and replication stress that lead to genomic instability.

MajSat-associated R loops are responsible for the genomic instability of perturbed p53-inactivated cells

R loops accumulating at repetitive sequences and associated with aberrant H3K9me3 are correlated with genomic instability in yeast, worms, and mammalian cells (Garcia-Muse and Aguilera, 2019; Zeller et al., 2016; Zhu et al., 2011). To determine the causative relationship within the cascade of events triggered by epigenetic perturbation in p53-inactivated cells, we experimentally reverted MajSat upregulation by transfection of Antago-MajSat. The antisense LNA reversed the increase in aneuploid cells (>4 n population; Figures 4A, 4B, S5A, and S5B). Micronucleus accumulation and mitotic pole duplication in different p53-inactivated experimental settings were significantly attenuated (Figures 4C, 4D, 4F, 4G, S5C, and S5D). Supporting a role of R loops in MajSat-promoted events, ectopic expression of RNAseH1 reduced R loop accumulation (Figure S5E) and recapitulated the effects of MajSat silencing on micronucleus and mitotic pole numbers (Figures 4E–4H, S5F, and S5G). These data directly implicated upregulation of satellite RNAs and consequent accumulation of R loops in the large-scale genomic instability produced by combination of epigenetic perturbation and p53 deficiency. Together with the characterization of heterochromatin instability in Figure 3, our data demonstrate that p53-deficient cells under epigenetic perturbation fail to maintain H3K9me in heterochromatin regions; the resultant increased transcription of satellites is a major mediator of genomic instability. Because p53 inactivation correlates with acquisition of genetic plasticity during PDAC progression, we suggest that instability of constitutive heterochromatin in response to (micro)environmental stressors might be the basis of genomic instability instated in permissive p53-mutant tumors.

Inadequate SAM levels underlie the aberrant response of p53-inactivated cells

p53 mutant tumors and p53-inactivated cells displayed reduced SAM levels (Figure 1). We hence hypothesize that p53 mutant cells do not cope with epigenetic stress because they are metabolically inadequate (i.e., reduced SAM levels). We wanted to determine a causative link between SAM levels and MajSat-associated genomic instability. Measurement of SAM intracellular concentration indicated that, in response to perturbation of DNA methylation by dC, cells increased the level of the methyl donor but, because of the lower basal level, p53-deficient cells failed to substantially achieve concentrations comparable with p53-proficient cells (Figure 5A). To compensate for this, we administered exogenous SAM to the culture medium of p53-deficient cells. Under this condition, upregulation of MajSat RNAs was reduced, and the level of H3K9 trimethylation was restored (Figures 5B and 5C). This suggested that SAM is indeed an essential factor to maintain the silencing heterochromatin state at satellite loci.

We next assessed whether the reduction in MajSat RNAs produced by exogenous SAM was accompanied by prevention of genomic instability. Micronucleus counts in p53-deficient cells were significantly reduced when the perturbation was associated with exogenous SAM administration (Figure 5D). These results indicate a role of intracellular SAM levels in chromosomal abnormalities, and they suggest that SAM, by reducing MajSat RNAs, prevented downstream deleterious consequences. Our data indicate that, because of low SAM levels, p53-deficient cells are metabolically inadequate to respond to stress, producing global epigenetic perturbation; therefore, they undergo heterochromatin instability-associated events that culminate in large-scale genomic instability.

p53 orchestrates a transcriptional program to sustain SAM synthesis in human PDAC

Finally, we explored how the p53-dependent transcriptional program influences the response to epigenetic perturbation. First, we ruled out direct transcriptional control of p53 on MajSat DNA; although a predicted binding site was identified (Figure S6A), the estimated binding affinity calculated by transcription factor affinity prediction (TRAP) analysis (Figure S6B) and ChIP-qPCR did not detect any p53 binding on MajSat-containing genomic loci (Figure S6C). We also ruled out an indirect transcriptional effect of p53, mediated by its transcriptional target p21 (Cdkn1a). p21 participates in the transcriptional repressor dimerization partner, RB-like, E2F and multi-vulval class B complex (DREAM) (Engeland, 2018). Silencing of p21 did not affect MajSat deregulation in perturbed and unperturbed cells in p53-proficient and
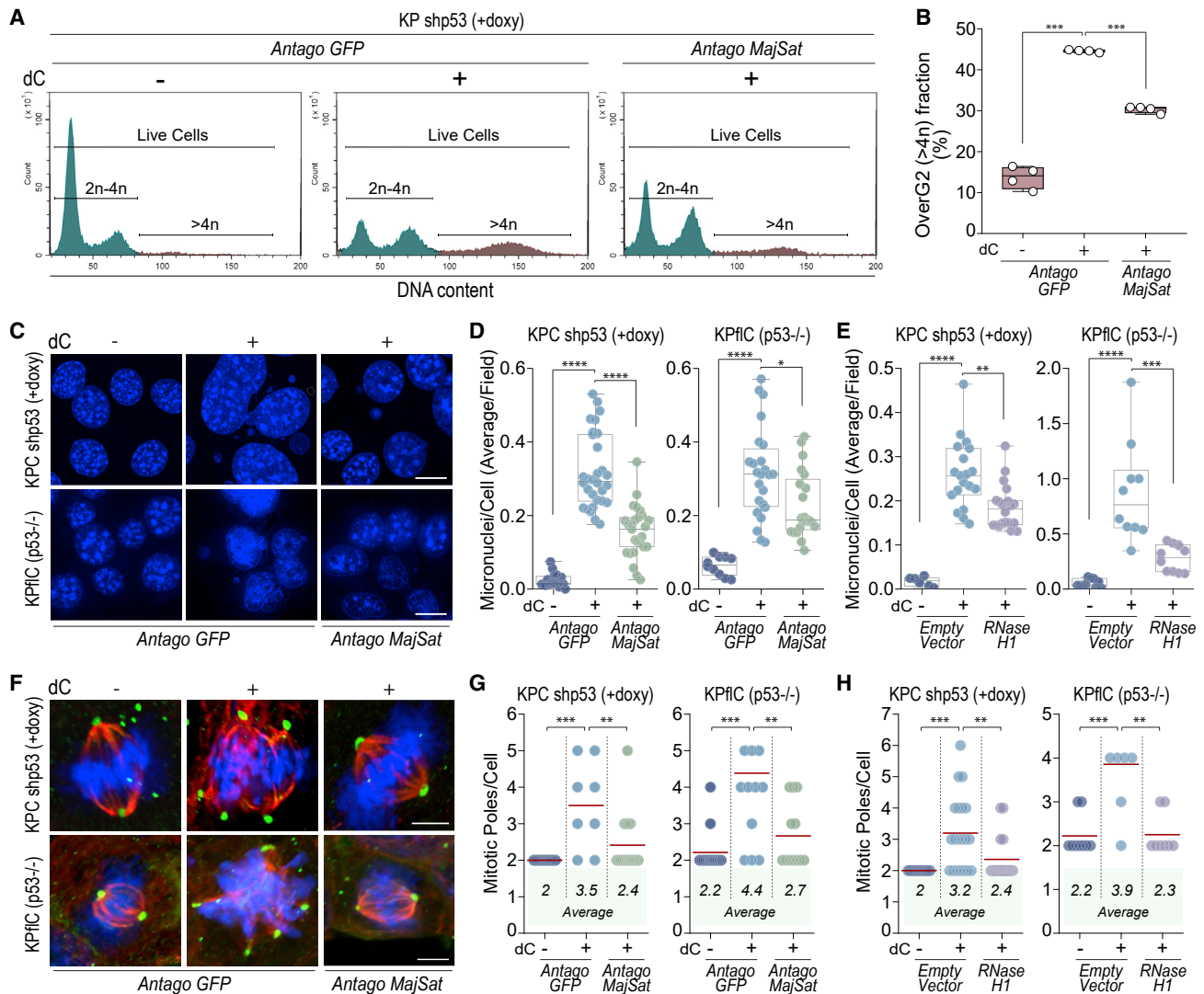
Figure 4. MajSat-associated R loops cause genomic instability in p53-deficient cells

(A) Histogram profiles of DNA content measured by propidium iodide FACS analysis in KPshp53 (+doxy) cells treated with dC after transfection with Antago-MajSat or Antago-GFP. A representative experiment of five independent biological replicates is shown.

(B) DNA content quantification (propidium iodide FACS analysis) for profiling of more than 4 n (aneuploid) cells (aneuploidy analysis). n = 4 independent biological replicates (dots). ***p < 0.001. The p values were calculated by two-way ANOVA with Tukey's correction.

(C) Micronucleus analysis by DAPI staining of p53-deficient cells treated with dC after transfection with Antago-MajSat or Antago-GFP. Scale bar, 5 μm.

(D and E) Micronuclear quantification of p53-deficient cells treated with dC after transfection with Antago-MajSat or Antago-GFP (D) or after transfection with an RNase H1 overexpression plasmid (E). Dots represent the results of quantification of an individual field. *p < 0.05, **p < 0.01, ***p < 0.001, ****p < 0.0001. The p values were calculated by ordinary one-way ANOVA with Tukey's correction.

(F) Mitotic pole analysis by α-tubulin (red) and γ-tubulin (green) IF staining of p53-deficient cells treated with dC after transfection with Antago-MajSat or Antago-GFP. Scale bar, 5 μm.

(G and H) Mitotic pole analysis (count per cell) in p53-deficient cells treated with dC after transfection with Antago-MajSat or Antago-GFP (G) or after transfection with an RNase H1 overexpression plasmid (H). Each dot represents an individual cell, and the red line indicates the average. *p < 0.05, **p < 0.01, ***p < 0.001, ****p < 0.0001. The p values were calculated by ordinary one-way ANOVA with Tukey's correction.

-deficient settings (Figures S6D and S6E). Next, we conducted an RNA sequencing (RNA-seq) analysis on p53-proficient and p53-deficient cells (Figures 5E and S6F–S6I), which revealed general dysregulation of cellular metabolic processes (Figure 5F). In particular, metabolic enzymes influencing one-carbon metabolism (*As3mt* [arsenite methyltransferase], *Shmt1* and *Shmt2*

[serine hydroxymethyltransferase 1 and 2], and *Gamt* [guanidinoacetate N-methyltransferase]), the sensor of SAM intracellular levels *Samtor* (*Bmt2*), and several metabolite transporters appeared to be regulated in a p53-dependent manner (Figures 5E–5G). This regulation was generally unrelated to exposure to DNA hypomethylation by dC treatment, confirming that they might
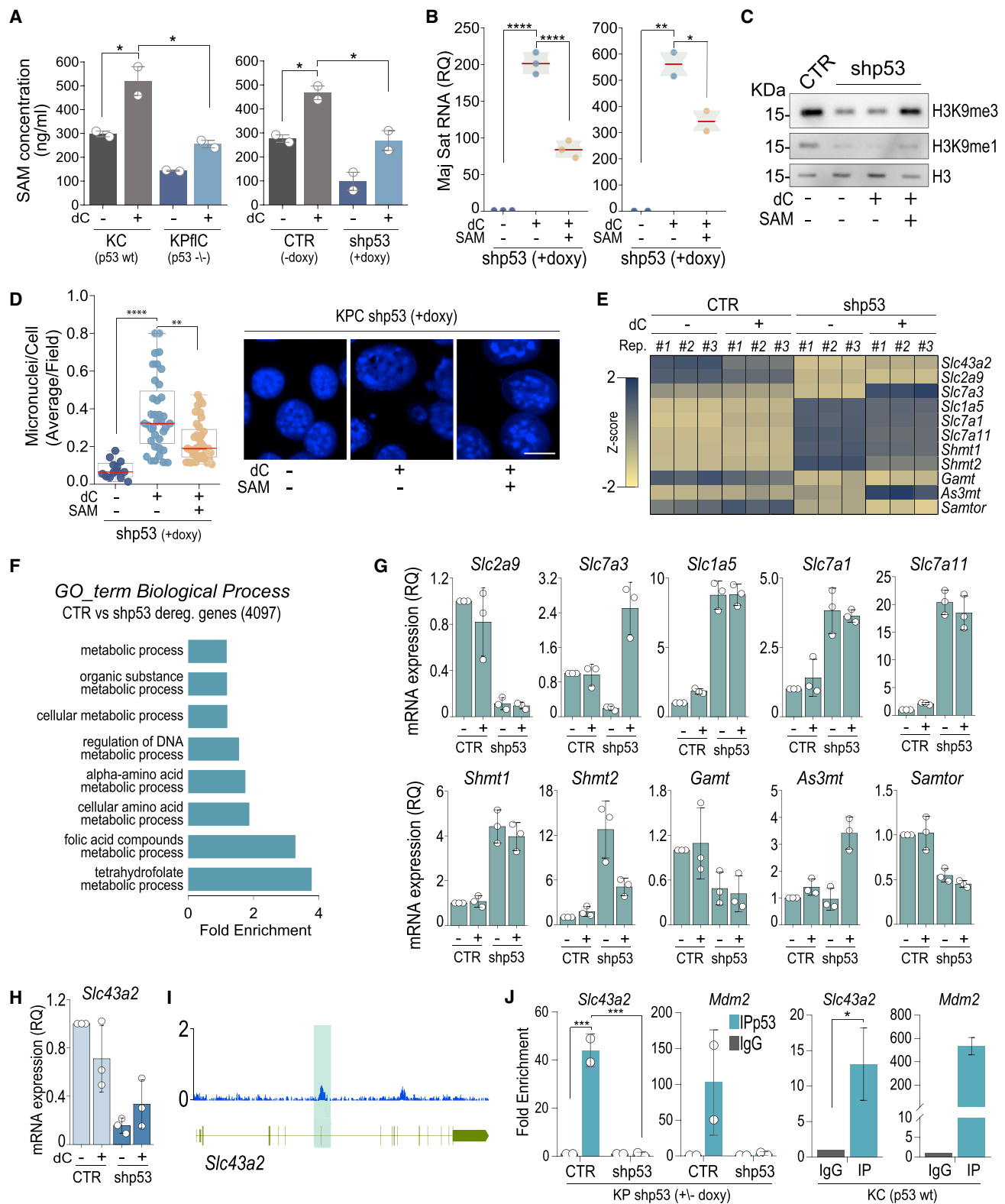
Figure 5. p53 controls a transcriptional program to support SAM synthesis

(A) Intracellular SAM concentration in dC-treated or untreated KC (p53 WT), KPflC (p53$^{-/-}$), KP CTR (−doxy), and KP shp53 (+doxy) cells. The p values were calculated by ordinary one-way ANOVA with Tukey's correction; n = 2 biological replicates (white dots). Data are presented as mean ± SEM.

underlie a pre-existing permissive condition associated with defective p53. The expression of several of these genes at the mRNA and protein levels was also often correlated with p53 status in human PDAC (Figures S7A and S7B). In this group, we noticed *Slc43a2*, a member of the L-amino acid transporter 3. Slc43a2 is the major transporter of extracellular methionine, a precursor of SAM synthesis, and is implicated in competition between cancer cells and T cells for methionine uptake and SAM-dependent histone methylation (Bian et al., 2020). *Slc43a2* appeared to be greatly downregulated after p53 depletion (Figure 5H), and p53 physical binding was identified in its gene locus by ChIP-seq experiments and confirmed by ChIP-qPCR analyses in our cell models (Figures 5I and 5J). Thus, p53 transcriptionally controls *Slc43a2* expression.

To directly implicate Slc43a2 in regulation of epigenetic stability and genomic integrity, we manipulated expression of Slc43a2. Silencing of Slc43a2 in cells expressing WT p53 (KPshp53 – doxycycline [doxy]) produced accumulation of MajSat RNAs accompanied by reduction of SAM concentration upon epigenetic perturbation (Figures 6A, S7C, and S7D). These cells also displayed accumulation of R loops and micronuclei (Figures 6B and 6C). Thus, depletion of Slc43a2 recapitulates the effects observed in p53 deficiency. We next overexpressed Slc43a2 to reintroduce its expression in a background where p53 was depleted (KPshp53 + doxy). Slc43a2 overexpression reduced the consequences of epigenetic pertubation in p53-deficient cells: with attenuation of MajSat transcription, accumulation of unscheduled R loops and micronuclei (Figures 6D–6F and S7E). Thus, Slc43a2 appears to have direct causative involvement in p53-mediated control of epigenetic and genomic integrity.

In support of a role of the p53/SLC43A2 axis in PDAC pathogenesis, expression of the mRNA and protein levels of this transporter were found to be correlated with p53 status in PDAC patients (Figure 6G). Differential expression of SLC43A2 was detected in malignant pancreatic tissue versus the normal counterpart (Figure 6H), correlating with the pattern of SAM abundance we revealed in human PDAC (Figure 1). The *SLC43A2* gene localizes in proximity to the *TP53* locus, and analysis of genomic data of PDAC patients are suggestive of a possible concurrent deletion of the gene codifying the transporter

in patients displaying the rare deletion events involving the p53 gene (Figure S7F). This indicates multiple levels of functional interactions of these two genes in cancer. Finally, analysis of the aneuploidy score indicated that, similar to p53 mutation or deletion, low mRNA expression of *SLC43A2* correlated with chromosomal abnormalities in PDAC patients (Figures 6I and 6J), supporting the link between genomic instability and this molecular axis. The SLC43A2 expression level can segregate PDAC patients into different prognostic groups (Figure 6K, left panel), and this effect is conserved in p53 WT and p53 mutant subcohorts (Figure 6K, center and left panels). These data, supported by the prognostic significance of SLC43A2, suggest that the p53/SLC43A2 axis might participate in PDAC pathogenesis by affecting SAM availability and predisposing individuals to conditions permissive for genomic instability.

This final set of data provides a mechanistic rationale for the link between p53 status, SAM, and genomic instability. It suggests that one role of p53 in genome maintenance is providing the metabolic basis for synthesis of SAM, a key metabolite for histone modifications and epigenetic homeostasis.

DISCUSSION

Dynamic control of histone methylation is influenced by alterations of SAM (Mentch et al., 2015). Thus, the SAM level is a critical decision-making factor functioning as a hub between metabolism and epigenetic regulation. Here we demonstrate that p53 inactivation leads to a reduction in SAM levels, exposing cells to a permissive status that underlies epigenetically associated mechanisms triggering genomic instability. We designed an experimental approach to mimic epigenetic perturbations (i.e., DNA demethylation) produced upon exposure to several stressors, including microenvironmental factors (metabolite supply, oxygen fluctuations), xenobiotics (tobacco smoke, alcohol, air pollution, etc.) or DNA-damaging chemotherapeutic drugs (doxorubicin, 5-FU, etc.) (Martin and Fry, 2018). Perturbed p53-deficient cells have SAM levels that are inadequate to prevent instability of repressive H3K9me3; this triggers transcription of repetitive satellite DNA as a consequence of relaxation of constitutive heterochromatin. Aberrant transcriptional control of noncoding repetitive regions leads to accumulation of an

(B) MajSat RNA level (qRT-PCR) in KP shp53 (+doxy) supplemented with exogenous SAM and treated with dC for 48 h (left) or 72 h (right). n = 3 biological replicates at 48 h and n = 2 biological replicates at 72 h (dots). *p < 0.05, **p < 0.01, ****p < 0.0001. The p values were calculated by RM one-way ANOVA with Fisher's LSD test.

(C) Western blot analysis of H3K9me3 and H3K9me1 in KP shp53 (+doxy) cells supplemented with exogenous SAM and treated with dC. Total H3 represents the loading control.

(D) Micronuclear quantification of p53-deficient cells treated with dC and supplemented with exogenous SAM. Dots represent the results of quantification of an individual field. **p < 0.01, ****p < 0.0001. The p values were calculated by ordinary one-way ANOVA with Tukey's correction. Micronuclei were visualized by DAPI staining. Scale bar, 20 μm.

(E) Heatmap of 11 significantly altered mRNAs selected from RNA-seq involved in amino acid transport and methionine metabolism.

(F) Gene Ontology analysis (GO_term) of genes differentially regulated in KP CTR (−doxy) versus KP shp53 (+doxy) cells.

(G) RNA-seq validation by qRT-PCR of mRNA represented in the heatmap in (E). Data are presented as mean ±SEM.

(H) *Slc43a2* mRNA level by qRT-PCR in KPshp53 (+doxy) and (−doxy) cells treated with dC or left untreated.

(G and H) n = 3 biological replicates (white dots); data are presented as mean ± SEM.

(I) ChIP sequencing (ChIP-seq) track showing p53 WT binding on the *SLC43A2* locus; the light blue band indicates the peak in the *SLC43A2* genomic locus.

(J) ChIP-qPCR analysis of p53 binding on Slc43a2 and Mdm2 genomic loci in KP CTR (−doxy), KP shp53 (+doxy), and KC cells. ***p < 0.001. The p values were calculated by ordinary one-way ANOVA with Tukey's correction; n = 2 biological replicates for KP shp53 and n = 2 technical replicates for KC p53 WT. Data are presented as mean ± SEM.
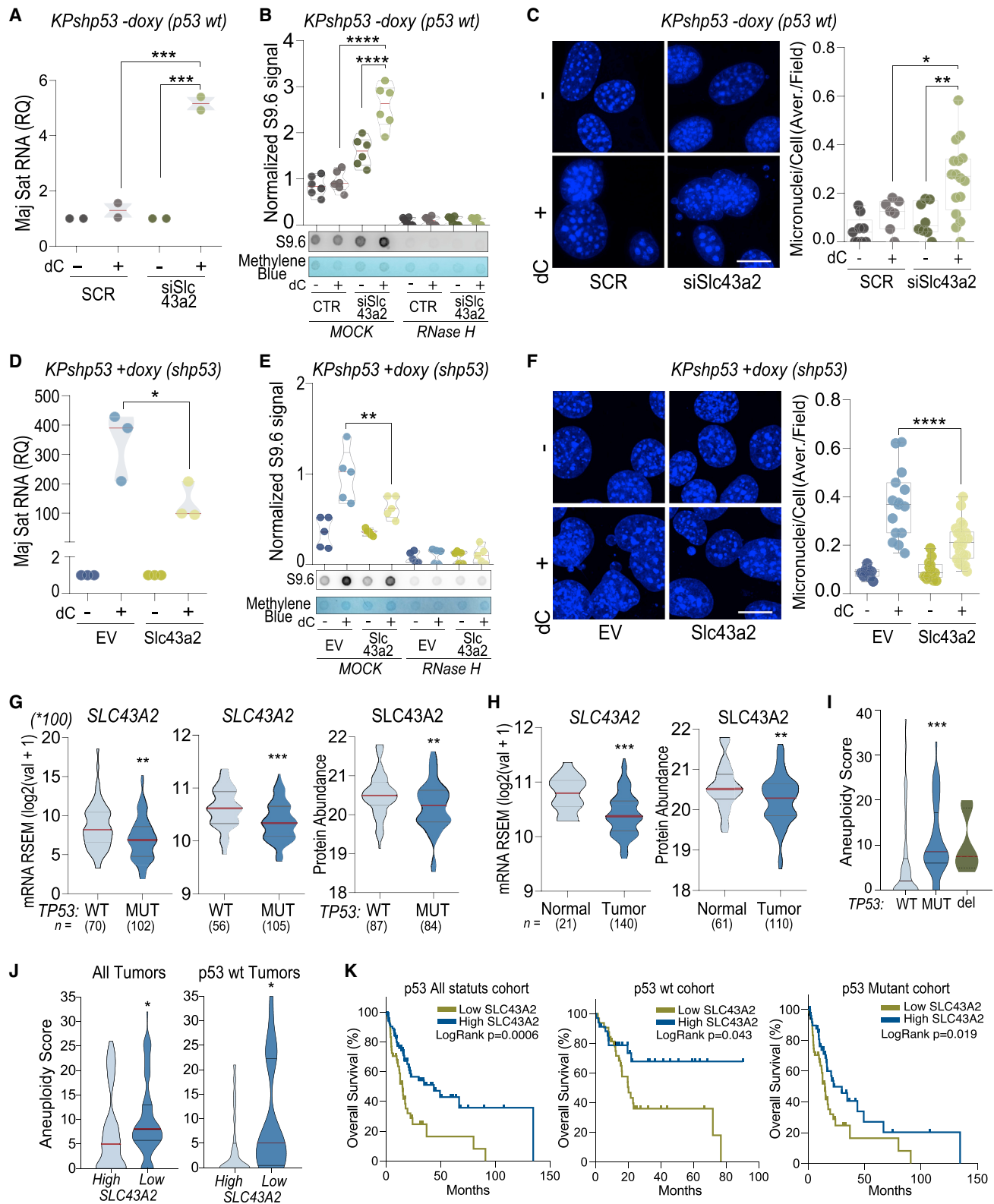
Figure 6. Slc43a2 has direct causative involvement in p53-mediated control of epigenetic and genomic integrity

(A) qRT-PCR of MajSat transcript in dC-treated and untreated p53-proficient KP CTR (−doxy) cells after Slc43a2 silencing. ***p < 0.001. The p values were calculated by ordinary one-way ANOVA with Tukey's correction; n = 2 biological replicates (dots).

(legend continued on next page)

unscheduled R loop associated with transcription-replication conflicts, replication stress, and chromosomal abnormalities. Cells expressing the missense mutant version of p53 (KPC^{R270H}, p53^{R270H}) reproduced the same effects as p53-depleted cells, indicating that this phenotype is generalizable to cancer-associated p53 inactivation. Thus, p53 deficiency leads to a state permissive for development of genomic instability upon exposure to epigenetic stressors.

The ability to control H3K9me stability is essential to preserve tissue integrity and healthy aging and prevent cancer (Methot et al., 2021; Nicetto et al., 2019; Zeller et al., 2016). Premature aging conditions, such as Werner syndrome, and inactivation of tumor suppressors, such as BRCA1, are associated with loss of H3K9me (Zhang et al., 2015; Zhu et al., 2011). H3K9me can act as an early barrier against Ras-mediated hyperproliferation in experimental models of oncogene-induced senescence of N-RAS^{G12D}-driven lymphoma (Braig et al., 2005). Upon exogenous perturbation, as a safeguard against exacerbated instability of heterochromatin as a consequence of loss of H3K9me3, preferential monomethylation events occur on H3K9 (Haws et al., 2020b). Perturbed p53-deficient cells, however, fail to reinstate epigenetic persistence, lacking the ability to introduce compensatory H3K9me1 or maintain H3K9me3. Lack of H3K9me results in global loss of heterochromatin stability, triggering derepression of satellite RNAs. Heterochromatin-encoded satellite RNAs are aberrantly transcribed in many cancer types, including PDAC (Ting et al., 2011), and their upregulation can directly promote cancer, resulting in unscheduled R-loop-dependent genomic instability (Zhu et al., 2018). We demonstrate that p53 loss exposes cells to metabolically associated epigenetic instability of constitutive heterochromatin that threatens genomic integrity. *Trp53*$^{-/-}$ mice can display birth defects and altered epigenetic methylation landscapes (Yi et al., 2012), and p53 cooperates with DNA methylation to prevent suicidal interferon-mediated cell death (Leonova et al., 2013) and

regulate the epigenetic pattern influencing gene expression (Morris et al., 2019).

We demonstrate that p53 transcriptionally controls a set of genes directly and indirectly affecting one-carbon metabolism, including the methionine transporter *Slc43a2*. We found direct causative involvement of Slc43a2 in p53-dependent epigenetic and genomic integrity because depletion of Slc43a2 recapitulates the effects of p53 loss, and reintroduction of this transporter in a p53 depleted background can reverse them. Remarkably, deregulation of SLC43A2 in cancer has been associated with altered methionine metabolism and histone methylation (Bian et al., 2020). Our data indicate a tight correlation between p53 status, SLC43A2 expression, and the prognosis of PDAC patients. Together with the analysis of SAM abundance in PDAC, this finding provides clinical relevance to our findings, indicating a mechanistic basis for the role of p53 in genomic integrity during progression of cancer.

Our findings demonstrate long-suspected crosstalk between p53 function and epigenetic integrity; we provide evidence that such crosstalk depends on metabolic control by p53, which affects epigenetic homeostasis and genomic integrity.

Limitations of the study

The contribution of the described p53-dependent regulation of epigenetic and genomic integrity to cancer development and progression remains to be determined. This work provides causative relationship between the p53/Slc43a2/SAM axis and genomic integrity, but the association with malignancy and patient prognosis is correlative, and direct causative links with cancer pathogenesis are not defined. Assessment of the influence of the p53/Slc43a2/SAM axis on cancer development and progression using injury-induced pancreatic cancer *in vivo* models could assist with addressing this open question and generalize our findings to environmentally triggered cancers.

(B) Dot blot analysis of S9.6 (R loop signal) of dC-treated or untreated p53-proficient KP CTR (−doxy) cells after Slc43a2 silencing. Treatment with RNAseH1 represents a control of specificity for the S9.6 signal. Methylene blue represents a loading control. Histograms report densitometry quantification of 6 biological replicates (dots). The p values were calculated by ordinary one-way ANOVA with Tukey's correction. ****p < 0.0001.

(C) Micronucleus count by DAPI staining on dC-treated or untreated p53-proficient KP CTR (−doxy) cells after Slc43a2 silencing. Left: representative microscopy images; scale bar, 5 μm. Dot plots show micronuclear quantification (count per cell); each dot represents a field. *p < 0.05, **p < 0.01. The p values were calculated by ordinary one-way ANOVA with Tukey's correction.

(D) qRT-PCR of the MajSat transcript in dC-treated or untreated p53-deficient KP CTR (+doxy) cells after Slc43a2 overexpression. **p < 0.01. The p values were calculated by ordinary one-way ANOVA with Tukey's correction; n = 3 biological replicates.

(E) Dot blot analysis of S9.6 (R loop signal) of dC-treated or untreated p53-deficient KP CTR (+doxy) cells after Slc43a2 overexpression. Treatment with RNAseH1 represents a control of specificity for the S9.6 signal. Methylene blue represents a loading control. Histograms report densitometry quantification of 5 independent biological replicates (dots). The p values were calculated by ordinary one-way ANOVA with Tukey's correction. ***p < 0.001.

(F) Micronucleus count by DAPI staining of dC-treated or untreated p53-deficient KP CTR (+doxy) cells after Slc43a2 overexpression. Left: representative images of microscopy images; scale bar, 20 μm. Dot plots show micronuclear quantification (count per cell); each dot represents a field. *p < 0.05, **p < 0.01. The p values were calculated by ordinary one-way ANOVA with Tukey's correction.

(G) SLC43a2 mRNA and protein levels in WT and mutant p53 human PDAC The left violin plot shows mRNA data from TCGA (Cbioportal). The center and right violin plots show mRNA and protein data from (Cao et al. 2021), respectively. **p < 0.01, ***p < 0.001. The p values were calculated with 2-tailed unpaired t test.

(H) SLC43A2 mRNA (left panel) and protein (right panel) analyses in N and T pancreatic tissue; source: (Cao et al. 2021). **p < 0.01, ***p < 0.001. The p values were calculated with 2-tailed unpaired t test.

(I) Tumor aneuploidy score in *TP53* WT versus mut (missense mutations) versus deleted (p53 loss) PDAC (left). ***p < 0.0001. The p values were calculated with ordinary one-way ANOVA with Tukey's correction.

(J) Tumor aneuploidy score in high vs. low SLC43A2 mRNA in the total cohort of PDAC (left) and in the subcohort of p53 WT PDAC (right). *p < 0.05. The p values were calculated with 2-tailed unpaired t test.

(K) Kaplan-Meier overall survival profile of PDAC patients stratified by low or high SLC43A2 mRNA levels in the total cohort of PDAC (left), in the subcohort of p53 WT PDAC (center), and in the subcohort of p53 mutant PDAC (right).

Cell Reports
Article

STAR★METHODS

Detailed methods are provided in the online version of this paper and include the following:

- KEY RESOURCES TABLE
- RESOURCE AVAILABILITY
  - Lead contact
  - Materials availability
  - Data and code availability
- EXPERIMENTAL MODEL AND SUBJECT DETAILS
  - Cell lines
  - Tissue microarray (TMA)
  - PDAC patients dataset
- METHOD DETAILS
  - Cell cultures and reagents
  - TMA immune histochemistry and analysis
  - DNA content and cell cycle analysis
  - Immunofluorescence (IF) and data analysis
  - DNA fibre assay
  - Proximity ligation assay (PLA)
  - Dot blot
  - Gene Ontology (GO) term enrichment analysis
  - Western blot
  - Intracellular SAM measurement
  - RT-qPCR
  - RNA fluorescent in situ hybridization (RNA FISH)
  - Chromatin immunoprecipitation (ChIP)
  - Metaphase chromosomes preparation
  - SAM supplementation
  - ATAC-seq (assay for transposase-accessible chromatin using sequencing)
  - RNA-seq
  - Live cell imaging
  - Bisulfite conversion reaction
  - Slc43a2 cloning
  - Bioinformatical analysis of PDAC datasets
- QUANTIFICATION AND STATISTICAL ANALYSIS

SUPPLEMENTAL INFORMATION

Supplemental information can be found online at https://doi.org/10.1016/j.celrep.2022.111568.

REFERENCES

Alonso-Curbelo, D., Ho, Y.J., Burdziak, C., Maag, J.L.V., Morris, J.P., 4th, Chandwani, R., Chen, H.A., Tsanov, K.M., Barriga, F.M., Luan, W., et al. (2021). A gene-environment-induced epigenetic program initiates tumorigenesis. Nature 590, 642–648. https://doi.org/10.1038/s41586-020-03147-x.

Aubrey, B.J., Kelly, G.L., Janic, A., Herold, M.J., and Strasser, A. (2018). How does p53 induce apoptosis and how does this relate to p53-mediated tumour suppression? Cell Death Differ. 25, 104–113. https://doi.org/10.1038/cdd.2017.169.

Bailey, J.A., Carrel, L., Chakravarti, A., and Eichler, E.E. (2000). Molecular evidence for a relationship between LINE-1 elements and X chromosome inactivation: the Lyon repeat hypothesis. Proc. Natl. Acad. Sci. USA 97, 6634–6639. https://doi.org/10.1073/pnas.97.12.6634.

Bian, Y., Li, W., Kremer, D.M., Sajjakulnukit, P., Li, S., Crespo, J., Nwosu, Z.C., Zhang, L., Czerwonka, A., Pawłowska, A., et al. (2020). Cancer SLC43A2 alters T cell methionine metabolism and histone methylation. Nature 585, 277–282. https://doi.org/10.1038/s41586-020-2682-1.

Brady, C.A., Jiang, D., Mello, S.S., Johnson, T.M., Jarvis, L.A., Kozak, M.M., Kenzelmann Broz, D., Basak, S., Park, E.J., McLaughlin, M.E., et al. (2011). Distinct p53 transcriptional programs dictate acute DNA-damage responses and tumor suppression. Cell 145, 571–583. https://doi.org/10.1016/j.cell.2011.03.035.

Braig, M., Lee, S., Loddenkemper, C., Rudolph, C., Peters, A.H.F.M., Schlegelberger, B., Stein, H., Dörken, B., Jenuwein, T., and Schmitt, C.A. (2005). Oncogene-induced senescence as an initial barrier in lymphoma development. Nature 436, 660–665. https://doi.org/10.1038/nature03841.

Bunz, F., Fauth, C., Speicher, M.R., Dutriaux, A., Sedivy, J.M., Kinzler, K.W., Vogelstein, B., and Lengauer, C. (2002). Targeted inactivation of p53 in human cells does not result in aneuploidy. Cancer Res. 62, 1129–1133.

Cao, L., Huang, C., Cui Zhou, D., Hu, Y., Lih, T.M., Savage, S.R., Krug, K., Clark, D.J., Schnaubelt, M., Chen, L., et al. (2021). Proteogenomic characterization of pancreatic ductal adenocarcinoma. Cell 184, 5031–5052.e26. https://doi.org/10.1016/j.cell.2021.08.023.

Daemen, A., Peterson, D., Sahu, N., McCord, R., Du, X., Liu, B., Kowanetz, K., Hong, R., Moffat, J., Gao, M., et al. (2015). Metabolite profiling stratifies pancreatic ductal adenocarcinomas into subtypes with distinct sensitivities to metabolic inhibitors. Proc. Natl. Acad. Sci. USA 112, E4410–E4417. https://doi.org/10.1073/pnas.1501605112.

Dai, Z., Ramesh, V., and Locasale, J.W. (2020). The evolving metabolic landscape of chromatin biology and epigenetics. Nat. Rev. Genet. 21, 737–753. https://doi.org/10.1038/s41576-020-0270-8.

Engeland, K. (2018). Cell cycle arrest through indirect transcriptional repression by p53: I have a DREAM. Cell Death Differ. 25, 114–132. https://doi.org/10.1038/cdd.2017.172.

García-Muse, T., and Aguilera, A. (2019). R loops: from physiological to pathological roles. Cell 179, 604–618. https://doi.org/10.1016/j.cell.2019.08.055.

Haws, S.A., Leech, C.M., and Denu, J.M. (2020a). Metabolism and the epigenome: a dynamic relationship. Trends Biochem. Sci. 45, 731–747. https://doi.org/10.1016/j.tibs.2020.04.002.

Haws, S.A., Yu, D., Ye, C., Wille, C.K., Nguyen, L.C., Krautkramer, K.A., Tomasiewicz, J.L., Yang, S.E., Miller, B.R., Liu, W.H., et al. (2020b).

Methyl-metabolite depletion elicits adaptive responses to support heterochromatin stability and epigenetic persistence. Mol. Cell 78, 210–223.e8. https://doi.org/10.1016/j.molcel.2020.03.004.

Hingorani, S.R., Petricoin, E.F., Maitra, A., Rajapakse, V., King, C., Jacobetz, M.A., Ross, S., Conrads, T.P., Veenstra, T.D., Hitt, B.A., Kawaguchi, Y., Johann, D., Liotta, L.A., Crawford, H.C., Putt, M.E., Jacks, T., Wright, C.V., Hruban, R.H., Lowy, A.M., and Tuveson, D.A. (2003). Preinvasive and invasive ductal pancreatic cancer and its early detection in the mouse. Cancer Cell. 4, 437–50. https://doi.org/10.1016/s1535-6108(03)00309-x.

Hirschey, M.D., DeBerardinis, R.J., Diehl, A.M.E., Drew, J.E., Frezza, C., Green, M.F., Jones, L.W., Ko, Y.H., Le, A., Lea, M.A., et al. (2015). Dysregulated metabolism contributes to oncogenesis. Semin. Cancer Biol. 35, S129–S150. https://doi.org/10.1016/j.semcancer.2015.10.002.

Jagannathan, M., Cummings, R., and Yamashita, Y.M. (2018). A conserved function for pericentromeric satellite DNA. Elife 7, e34122. https://doi.org/10.7554/eLife.34122.

Janssen, A., Colmenares, S.U., and Karpen, G.H. (2018). Heterochromatin: guardian of the genome. Annu. Rev. Cell Dev. Biol. 34, 265–288. https://doi.org/10.1146/annurev-cellbio-100617-062653.

Kastenhuber, E.R., and Lowe, S.W. (2017). Putting p53 in context. Cell 170, 1062–1078. https://doi.org/10.1016/j.cell.2017.08.028.

Kawabata, T., Luebben, S.W., Yamaguchi, S., Ilves, I., Matise, I., Buske, T., Botchan, M.R., and Shima, N. (2011). Stalled fork rescue via dormant replication origins in unchallenged S phase promotes proper chromosome segregation and tumor suppression. Mol. Cell 41, 543–553. https://doi.org/10.1016/j.molcel.2011.02.006.

Kishikawa, T., Otsuka, M., Yoshikawa, T., Ohno, M., Ijichi, H., and Koike, K. (2016). Satellite RNAs promote pancreatic oncogenic processes via the dysfunction of YBX1. Nat. Commun. 7, 13006. https://doi.org/10.1038/ncomms13006.

Kruiswijk, F., Labuschagne, C.F., and Vousden, K.H. (2015). p53 in survival, death and metabolic health: a lifeguard with a licence to kill. Nat. Rev. Mol. Cell Biol. 16, 393–405. https://doi.org/10.1038/nrm4007.

Laptenko, O., and Prives, C. (2017). p53: master of life, death, and the epigenome. Genes Dev. 31, 955–956. https://doi.org/10.1101/gad.302364.117.

Leonova, K.I., Brodsky, L., Lipchick, B., Pal, M., Novototskaya, L., Chenchik, A.A., Sen, G.C., Komarova, E.A., and Gudkov, A.V. (2013). p53 cooperates with DNA methylation and a suicidal interferon response to maintain epigenetic silencing of repeats and noncoding RNAs. Proc. Natl. Acad. Sci. USA 110, E89–E98. https://doi.org/10.1073/pnas.1216922110.

Li, L.C., and Dahiya, R. (2002). MethPrimer: designing primers for methylation PCRs. Bioinformatics. 18, 1427–31. https://doi.org/10.1093/bioinformatics/18.11.1427.

Lungu, C., Pinter, S., Broche, J., Rathert, P., and Jeltsch, A. (2017). Modular fluorescence complementation sensors for live cell detection of epigenetic signals at endogenous genomic sites. Nat. Commun. 8, 649. https://doi.org/10.1038/s41467-017-00457-z.

Martin, E.M., and Fry, R.C. (2018). Environmental influences on the epigenome: exposure- associated DNA methylation in human populations. Annu. Rev. Publ. Health 39, 309–333. https://doi.org/10.1146/annurev-publhealth-040617-014629.

Mentch, S.J., Mehrmohamadi, M., Huang, L., Liu, X., Gupta, D., Mattocks, D., Gómez Padilla, P., Ables, G., Bamman, M.M., Thalacker-Mercer, A.E., et al. (2015). Histone methylation dynamics and gene regulation occur through the sensing of one-carbon metabolism. Cell Metabol. 22, 861–873. https://doi.org/10.1016/j.cmet.2015.08.024.

Methot, S.P., Padeken, J., Brancati, G., Zeller, P., Delaney, C.E., Gaidatzis, D., Kohler, H., van Oudenaarden, A., Großhans, H., and Gasser, S.M. (2021). H3K9me selectively blocks transcription factor activity and ensures differentiated tissue integrity. Nat. Cell Biol. 23, 1163–1175. https://doi.org/10.1038/s41556-021-00776-w.

Morris, J.P., 4th, Yashinskie, J.J., Koche, R., Chandwani, R., Tian, S., Chen, C.C., Baslan, T., Marinkovic, Z.S., Sánchez-Rivera, F.J., Leach, S.D., et al. (2019). alpha-Ketoglutarate links p53 to cell fate during tumour suppression. Nature 573, 595–599. https://doi.org/10.1038/s41586-019-1577-5.

Nicetto, D., Donahue, G., Jain, T., Peng, T., Sidoli, S., Sheng, L., Montavon, T., Becker, J.S., Grindheim, J.M., Blahnik, K., et al. (2019). H3K9me3-heterochromatin loss at protein-coding genes enables developmental lineage specification. Science 363, 294–297. https://doi.org/10.1126/science.aau0583.

Olive, K.P., Tuveson, D.A., Ruhe, Z.C., Yin, B., Willis, N.A., Bronson, R.T., Crowley, D., and Jacks, T. (2004). Mutant p53 gain of function in two mouse models of Li-Fraumeni syndrome. Cell 119, 847–860. https://doi.org/10.1016/j.cell.2004.11.004.

Probst, A.V., Okamoto, I., Casanova, M., El Marjou, F., Le Baccon, P., and Almouzni, G. (2010). A strand-specific burst in transcription of pericentric satellites is required for chromocenter formation and early mouse development. Dev. Cell 19, 625–638. https://doi.org/10.1016/j.devcel.2010.09.002.

Quinet, A., Carvajal-Maldonado, D., Lemacon, D., and Vindigni, A. (2017). DNA fiber analysis: mind the gap. Methods Enzymol. 591, 55–82. https://doi.org/10.1016/bs.mie.2017.03.019.

Ramirez, P., Crouch, R.J., Cheung, V.G., and Grunseich, C. (2021). R-Loop Analysis by Dot-Blot. J Vis Exp. 22. https://doi.org/10.3791/62069.

Sanderson, S.M., Gao, X., Dai, Z., and Locasale, J.W. (2019). Methionine metabolism in health and cancer: a nexus of diet and precision medicine. Nat. Rev. Cancer 19, 625–637. https://doi.org/10.1038/s41568-019-0187-8.

Schneider, C.A., Rasband, W.S., and Eliceiri, K.W. (2012). NIH Image to ImageJ: 25 years of image analysis. Nat Methods. 9, 671–5. https://doi.org/10.1038/nmeth.2089.

Ting, D.T., Lipson, D., Paul, S., Brannigan, B.W., Akhavanfard, S., Coffman, E.J., Contino, G., Deshpande, V., Iafrate, A.J., Letovsky, S., et al. (2011). Aberrant overexpression of satellite repeats in pancreatic and other epithelial cancers. Science 331, 593–596. https://doi.org/10.1126/science.1200801.

Valente, L.J., Gray, D.H.D., Michalak, E.M., Pinon-Hofbauer, J., Egle, A., Scott, C.L., Janic, A., and Strasser, A. (2013). p53 efficiently suppresses tumor development in the complete absence of its cell-cycle inhibitory and proapoptotic effectors p21, Puma, and Noxa. Cell Rep. 3, 1339–1345. https://doi.org/10.1016/j.celrep.2013.04.012.

Weissmueller, S., Manchado, E., Saborowski, M., Morris, J.P., 4th, Wagenblast, E., Davis, C.A., Moon, S.H., Pfister, N.T., Tschaharganeh, D.F., Kitzing, T., et al. (2014). Mutant p53 drives pancreatic cancer metastasis through cell-autonomous PDGF receptor beta signaling. Cell 157, 382–394. https://doi.org/10.1016/j.cell.2014.01.066.

Wilson, A.S., Power, B.E., and Molloy, P.L. (2007). DNA hypomethylation and human diseases. Biochim. Biophys. Acta 1775, 138–162. https://doi.org/10.1016/j.bbcan.2006.08.007.

Yang, W., Xia, Y., Cao, Y., Zheng, Y., Bu, W., Zhang, L., You, M.J., Koh, M.Y., Cote, G., Aldape, K., et al. (2018). EGFR-induced and PKCepsilon monoubiquitylation-dependent NF-kappaB activation upregulates PKM2 expression and promotes tumorigenesis. Mol. Cell 69, 347. https://doi.org/10.1016/j.molcel.2017.12.034.

Yi, L., Lu, C., Hu, W., Sun, Y., and Levine, A.J. (2012). Multiple roles of p53-related pathways in somatic cell reprogramming and stem cell differentiation. Cancer Res. 72, 5635–5645. https://doi.org/10.1158/0008-5472.CAN-12-1451.

Zeller, P., Padeken, J., van Schendel, R., Kalck, V., Tijsterman, M., and Gasser, S.M. (2016). Histone H3K9 methylation is dispensable for Caenorhabditis elegans development but suppresses RNA:DNA hybrid-associated repeat instability. Nat. Genet. 48, 1385–1395. https://doi.org/10.1038/ng.3672.

Zhang, W., Li, J., Suzuki, K., Qu, J., Wang, P., Zhou, J., Liu, X., Ren, R., Xu, X., Ocampo, A., et al. (2015). Aging stem cells. A Werner syndrome stem cell model unveils heterochromatin alterations as a driver of human aging. Science 348, 1160–1163. https://doi.org/10.1126/science.aaa1356.

Zhang, Y., Liu, T., Meyer, C.A., Eeckhoute, J., Johnson, D.S., Bernstein, B.E., Nusbaum, C., Myers, R.M., Brown, M., Li, W., and Liu, X.S. (2008). Model-based analysis of ChIP-Seq (MACS). Genome Biol. *9*, R137. https://doi.org/10.1186/gb-2008-9-9-r137.

Zhu, Q., Hoong, N., Aslanian, A., Hara, T., Benner, C., Heinz, S., Miga, K.H., Ke, E., Verma, S., Soroczynski, J., et al. (2018). Heterochromatin-encoded satellite RNAs induce breast cancer. Mol. Cell *70*, 842–853.e7. https://doi.org/10.1016/j.molcel.2018.04.023.

Zhu, Q., Pao, G.M., Huynh, A.M., Suh, H., Tonnu, N., Nederlof, P.M., Gage, F.H., and Verma, I.M. (2011). BRCA1 tumour suppression occurs via hetero-chromatin-mediated silencing. Nature *477*, 179–184. https://doi.org/10.1038/nature10371.

STAR★METHODS

KEY RESOURCES TABLE

REAGENT or RESOURCE	SOURCE	IDENTIFIER
Antibodies		
p53 (DO-1)	Santa Cruz	Cat.#sc-126 RRID:AB_628082
Novocastra™ Liquid Rabbit Polyclonal Antibody p53 Protein (CM5)	Leica Biosystem	Cat#NCL-L-p53-CM5p RRID:AB_2895247
S-Adenosylmethionine monoclonal antibody, clone 84-3	Abnova	Cat.#MAB12270
Monoclonal Anti-α-Tubulin antibody produced in mouse	Sigma-Aldrich	Cat#T9026 RRID:AB_477593
Anti-γ-Tubulin antibody produced in rabbit	Sigma-Aldrich	Cat#T3559 RRID:AB_477575
Anti-DNA-RNA Hybrid Antibody, clone S9.6	Merck (Sigma-Aldrich)	Cat#MABE1095 RRID:AB_2861387
HP1 (E-6)	Santa Cruz	Cat.# sc-515341
Recombinant Anti-Histone H3 (trimethyl K9) [EPR16601]	Abcam	Cat#ab176916 RRID:AB_2797591
Recombinant Anti-Histone H3 (monomethyl K9) [EPR16989]	Abcam	Cat#ab176880 RRID:AB_2751009
Histone H3K4me3 antibody (pAb)	Active Motif	Cat#39159 RRID:AB_2615077
Anti-trimethyl-Histone H3 (Lys27) Antibody	Merck (Sigma-Aldrich)	Cat#07-449 RRID:AB_310624
Histone H3K36me3 antibody (pAb)	Active Motif	Cat#61902 RRID:AB_2615073
Anti-Histone H3 antibody [mAbcam 10799]	Abcam	Cat#ab10799 RRID:AB_470239
Purified Mouse Anti-BrdU (B44)	BD Biosciences	Cat#347580 RRID:AB_10015219
Anti-BrdU antibody [BU1/75 (ICR1)]	Abcam	Cat# ab6326 RRID:AB_305426
Goat anti-Mouse IgG1 Cross-Adsorbed Secondary Antibody, Alexa Fluor™ 546	Thermo Fisher	Cat#A21123 RRID:AB_2535765
Chicken anti-Rat IgG (H+L) Cross-Adsorbed Secondary Antibody, Alexa Fluor™ 488	Thermo Fisher	Cat# A21470 RRID:AB_2535873
PCNA (PC10)	Santa Cruz	Cat.#sc-56 RRID:AB_628110
Anti-phospho-Histone H2A.X (Ser139) JBW301	Merck (Sigma-Aldrich)	Cat#05-636 RRID:AB_309864
Anti-GAPDH antibody, Mouse monoclonal	Sigma-Aldrich	Cat#G8795 RRID:AB_1078991
Monoclonal Anti-β-Actin antibody produced in mouse	Sigma-Aldrich	Cat#A5441 RRID:AB_476744
Biological samples		
Pancreatic cancer tissue array	US Biomax, Inc.	PA807
Pancreatic cancer tissue array	US Biomax, Inc.	PA241d
Chemicals, peptides, and recombinant proteins		
5-Aza-2′-deoxycytidine	Sigma-Aldrich	Cat#A3656
5-Iodo-2′-deoxyuridine	Sigma-Aldrich	Cat#I7125
5-Chloro-2′-deoxyuridine	Sigma-Aldrich	Cat#C6891
S-(5′-Adenosyl)-L-methionine chloride dihydrochloride	Sigma-Aldrich	Cat#A7007
DNase I	Sigma-Aldrich	Cat#AMPD1

(Continued on next page)

Continued

REAGENT or RESOURCE	SOURCE	IDENTIFIER
Stellaris® RNA FISH Hybridization buffer	Biosearch Technologies	Cat#SMF-HB1-10
Stellaris® RNA FISH Wash buffer A	Biosearch Technologies	Cat#SMF-WA1-60
Stellaris® RNA FISH Wash buffer B	Biosearch Technologies	Cat#SMF-WB1-20
Critical commercial assays		
UltraTek HRP Anti-Polyvalent (DAB) Staining System	HistoLine Laboratories	Cat#AMF080
Mouse S-Adenosylmethionine (SAM) ELISA Kit	MyBioSource	Cat#MBS2603023
Deposited data		
Raw and analyzed RNAseq and ATACseq data	This study	GSE207880
ChIPseq (referred to Figure 5I)	https://chip-atlas.org/	SRX2170272
Metabolic profiling of PDAC (referred to Figure 1E)	https://doi.org/10.1073/pnas.1501605112	Excel table available for download at the paper web page
Proteomic and transcriptomic data (referred to Figures 6G and 6H)	https://doi.org/10.1016/j.cell.2021.08.023	http://www.linkedomics.org/data_download/CPTAC-PDAC/
Genomic data and survival analysis (referred to Figures 6G and 6I–6K)	https://www.cbioportal.org/	N/A
Experimental models: Cell lines		
KPshp53: *dx1-cre;LSL-Kras^G12D^;Col1a1-TRE-shp53-shRenilla;Rosa26-CAGs-LSL-rtTA-IRES-mKate2*	Scott Lowe - Morris et al. (2019)	N/A
KPflC: *Pdx-Cre, LSL-Kras^G12D/+^, LSL-trp53^loxP/+^*	Scott Lowe - Weissmueller et al. (2014)	N/A
KC: *Pdx1-Cre; KrasG12D/+*	David Tuveson - Hingorani et al., 2003	N/A
KPC270: tr*p53^R270H/−^*	Jennifer Morton - Olive et al. (2004)	N/A
NIH/3T3	ATCC	Cat#CRL-1658 RRID:CVCL_0594
C2C12	ATCC	Cat#CRL-1772 RRID:CVCL_0188
Oligonucleotides		
qRT-qPCR primer sequences		
Gamt	5′-CACGCACCTGCAAATCCTG-3′	5′-TACCGAAGCCCACTTCCAAGA-3′
Shmt1	5′-GGATGATAATGGGGCGTATCTCA-3′	5′-GTCTTGTGGGTTGTAGTGGTC-3′
Shmt2	5′-TGACTATGCACGCATGAGAGA-3′	5′-ATCCGCGTACTTGAAAGGGG-3′
As3mt	5′-GGGAATGTACTGAAGACATCTGC-3′	5′-CCACAGCCATAATACCTCGAACT-3′
Slc7a1	5′-CTCTCTCTGCGCACTTTCCA-3′	5′-CTGAGGTCACAGTGGCGATT-3′
Slc43a2	5′-TGCACCGCTGTGTTGGAAA-3′	5′-CCGTGCTGTTAGTGACATTCTC-3′
Slc2a9	5′-TTGCTTTAGCTTCCCTGATGTG-3′	5′-GAGAGGTTGTACCCGTAGAGG-3′
Slc7a3	5′-TGAGCACCCTCGACTTAGTG-3′	5′-CACAATGGATGGTCCTGCTTTA-3′
Slc1a5	5′-TACCGCAATCCTGTATCCAGC-3′	5′-CACCAAAGACGATAGCGAAGAC-3′
Slc7a11	5′-GGCACCGTCATCGGATCAG-3′	5′-CTCCACAGGCAGACCAGAAAA-3′
Samtor	5′-GAGGGTGAAGGTCGCATTGA-3′	5′-TGCACGTTTAAGGCTGGAGT-3′
MajSat	5′-GACGACTTGAAAAATGACGAAATC-3′	5′-CATATTCCAGGTCCTTCAGTGTGC-3′
Tbp	5′-TTGGCTAGGTTTCTGCGGTC-3′	5′-TGGAAGGCTGTTGTTCTGGT-3′
Cdkn1a	5′-CGGTGTCAGAGTCTAGGGGA-3′	5′-ATCACCAGGATTGGACATGG-3′
ChIP-qPCR primer sequences		
Maj Sat	5′-CCAGGTCCTACAGTGTGCATTTC-3′	5′-CGTGAAATATGGCGAGGAAAACT-3′
Gapdh	5′-GGGTTCCTATAAATACGGACTGC-3′	5′-CTGGCACTGCACAAGAAGA-3′
Mdm2	5′-TGATCTAGCTCTTCCTGTGG-3′	5′-GAGCTGTCCCTTACCTGGAG-3′
Slc43a2	5′-ATGATATGTGCTGAGGGCTG-3′	5′-GAAAAGTCTGCATAGGCCAGG-3′
Bisulfite assay PCR primer sequences		
Unmethylated MajSat	5′-TGAGAAATTTGAAAATTATGGA-3′	5′-TTTCTTACCATACTCCACATC-3′

(Continued on next page)

Continued

REAGENT or RESOURCE	SOURCE	IDENTIFIER
LNA oligo sequences		
LNA DNA GAPMER MAJ 1	5′-ACATCCACTTGACGACTTG-3′	339512 LG00220660-DFA
LNA DNA GAPMER MAJ 2	5′-TATTTCACGTCCTAAAGTG-3′	339512 LG00220661-DFA
LNA DNA GAPMER GFP	5′-GAGAAAGTGTGACAAGTG-3′	339512 LG00220662-DFA
Cloning PCR primer sequences		
NheI-Kozak-FLAG-mSlc43a2 fw	5′-ggccGCTACGGAGGAGATCTGCCGCCGCGATCGCCATGGATTACAAGGA TGAC GACGATAAGATGGCGCCCACCCTGGCCACTGC-3′	
HindIII-mSlc43a2 rev	5′-ggccAAGCTTCTACACGAAAGCCTCCCGGTTGG-3′	
Recombinant DNA		
FLAG-MaSat-NLS-ZF-18-mVenusN	Albert Jeltsch - Lungu et al., 2017	N/A
FLAG-mVenusC-14-HP1b-Chromo	Albert Jeltsch - Lungu et al., 2017	N/A
pcDNA3.1-mSlc43a2	This study	N/A
pcDNA3.1 (empty vector)	Addgene	Cat#V790-20
DUAL-tandem-Tomato	Addgene	Cat# 48735
Software and algorithms		
FIJI - ImageJ	Schneider et al., 2012	https://imagej.nih.gov/ij/
GraphPad Prism 8.0.1	GraphPad Software	https://www.graphpad.com/scientific-software/prism/
MethPrimer	Urogene	https://www.urogene.org/methprimer/
Integrated Genome Browser (IGB)	BioViz	https://bioviz.org/
Kaluza software analysis 2.1	BECKMAN COULTER	https://www.beckman.it/flow-cytometry/software/kaluza/downloads
Nucleotide BLAST	NCBI	https://blast.ncbi.nlm.nih.gov/Blast.cgi
NIS-Elements imaging software	Nikon	https://www.microscope.healthcare.nikon.com/products/software/nis-elements

RESOURCE AVAILABILITY

Lead contact

Further information and requests for resources and reagents should be directed to and will be fulfilled by the lead contact, Ivano Amelio (ivano.amelio@uni-konstanz.de).

Materials availability

The unique material generated in this study (see key resources table) is available upon request from the lead contact without any restriction.

Data and code availability

- RNAseq and ATACseq generated in this study have been deposited at GEO and are publicly available. Accession numbers are listed in the key resources table.
- This paper does not report original code.
- Any additional information required to reanalyse the data reported in this paper is available from the lead contact upon request.

EXPERIMENTAL MODEL AND SUBJECT DETAILS

Cell lines

KPshp53, KPflC, and KC cells were kindly donated by Scott W Lowe. KPC270 (Olive et al., 2004) were kindly donated by Jennifer Morton. KPshp53 cells derive from PDAC that developed in a *Pdx1-cre;LSL-Kras^{G12D};Col1a1-TRE-shp53-shRenilla;Rosa26-CAGs-LSL-rtTA-IRES-mKate2* mice (Morris et al., 2019). KPflC cells derive from PDAC that developed in a *Pdx-Cre, LSL-Kras^{G12D/+}, LSL-trp53^{loxP/+}* (Weissmueller et al., 2014). KC cells derive from PDAC that developed in a *Pdx1-Cre; Kras^{G12D/+}*

([Hingorani et al., 2003](#)). C2C12 and NIH/3T3 has been purchased from ATCC (see [key resources table](#) for catalogue product number). All the murine PDAC cell lines have been authenticated as described in the source papers (references above); we also confirm p53 status by RT-qPCR or western blot.

Tissue microarray (TMA)

Human pancreatic cancer tissues array (#PA807; #PA241d) where purchased from US Biomax (Rockville, MD, USA), that handled ethical committee approval and informed consent from the subjects. Information related to the tissue array, including informed consent and human subjects age, sex, and tumour developmental stage are available at the following links: https://www.biomax.us/, https://www.biomax.us/tissue-arrays/Pancreas/PA807, https://www.biomax.us/tissue-arrays/Pancreas/PA241d.

PDAC patients dataset

Publicly available datasets from [Cao et al. (2021)](#) (see also [key resources table](#)) were used to compute correlations analyses of transcriptomic and proteomic data of PDAC patients. A total of 140 cases with pancreatic cancer were evaluated and included in this study; all the information related to the patients (e.g. sex, age, tumour features) are free available at the source paper. Institutional review boards reviewed protocols and consent documentation adhering to the Clinical Proteomic Tumour Analysis Consortium (CPTAC) guidelines.

METHOD DETAILS

Cell cultures and reagents

All the cell lines were grown in DMEM (10% FBS Gibco; penicillin–streptomycin 2units/mL) at 37°C, 5% CO_2. KPshp53 were maintained in 1 μg/mL doxycycline to keep off p53 through doxy-dependent shRNA against Trp53; to allow p53 expression the doxycycline was removed 48 h before further procedure; KPshp53 were propagated on collagen-coated plates (PurCol, Advanced Biomatrix, 0.1 mg/mL); to perturbate DNA methylation, 24–72 h of 10μM dC treatment was used (Sigma, 5-Aza-2′-deoxycytidine, #A3656). siRNA transfection was performed with Lipofectamine RNAiMAX (Invitrogen) using 60 nM of pre-designed *Trp53* siRNA (Ambion, #s75472), *Slc43a2* siRNA (Thermo Fisher, #4390771, siRNA ID s103265), *Cdkn1a* siRNA (Thermo Fisher, #4390771, ID s63812), or Silencer Negative Control siRNA (Ambion). For overexpression experiment 4 μg/6 cm dish of Slc43a2 expressing vector or the control empty vector (see cloning details below) were transfected using Lipofectamine™ 3000 Transfection Reagent (Thermo, #L3000015) following the manufacturer's instructions. Antisense locked nucleic acid (LNA)-DNA (gapmers) oligonucleotides against Major Satellite transcript were purchased from QIAGEN; two sequences were mixed to obtain an efficient knockdown and an antisense LNA-DNA gapmer against GFP was used as scramble sequence ([Probst et al., 2010](#)) (see [key resources table](#)). Cells were transfected at 60% confluence with 200 nM gapmers mix (100 + 100 nM) by using Lipofectamine™ RNAiMAX Transfection Reagent (Thermo, #13778-150) following the manufacturer's instructions. RNaseH1 was transfected using Lipofectamine™ 3000 Transfection Reagent (Thermo, #L3000015) following the manufacturer's instructions; 6 h post-transfection the medium was replaced and the cells were treated with dC for 48–72 h and then collected for follow-up analysis. Micronuclei, R-loops, and mitotic poles imaging and analysis were performed as described below on 20–40 random field per sample. Cell cycle analysis and DNA content after Major Satellite knockdown (n = 4 biological replicates) were performed and analyzed as described below.

TMA immune histochemistry and analysis

Slides were incubated at 58°C for 1 h, dewaxed by Bio-Clear washing (Bio-Optica) and rehydrated by 96%, 96%, 70% ethanol incubations; after endogenous peroxide blocking, antigen retrieval was performed by boiling in 0.01 M Sodium Citrate Buffer pH 6.0; primary antibody incubation were performed overnight at 4°C (anti-p53 Santa Cruz #sc-126; anti-SAM Abnova #MAB12270); immunohistochemistry were performed by using UltraTek HRP Anti-Polyvalent (DAB) Staining System (Histo-Line Laboratories, #AMF080) following the manufacturer's instruction; images were acquired with Leica DM6 B microscope and Leica DCF 7000 T camera. Samples were scored in a blinded manner by a pathologist using a semi-quantitative method; cases were analyzed for staining intensity, which was scored as 0 (not detected), 1+ (weak), 2+ (intermediate), and 3+ (strong); for each case, the H-score was calculated by multiplying the percentage of positive cells (0%–100%) by the intensity (0–3).

DNA content and cell cycle analysis

Cells and supernatant were collected and fixed with methanol:acetone (4:1) at 4°C; after 20 min RNaseA incubation at room temperature (RT), samples were labeled with propidium iodide (70 μg/mL) for 4 h at RT and acquired with CytoFLEX (Beckman Coulter, 20000 events/sample). Cell cycle analysis was performed using Kaluza software analysis 2.1; subG1 population was determined considering all the events with a PI content lower than G1 (excluding debris); DNA content analysis was performed dividing the live cell population in two groups: "2 n-4 n" includes all the cells identified by the aforementioned cell cycle analysis (2n = G1, 4n = G2/M); ">4n" includes all the cells showing a PI content higher than G2/M.

Immunofluorescence (IF) and data analysis

Cells were seeded on glass slides, treated as described before and fixed with Paraformaldehyde (PFA) 4% in PBS (phosphate-buffered saline, HP1 and H3K9me3), or 10′ methanol and 1′ acetone on ice (S9.6, R-loops), or methanol:acetone 50:50 on ice (alpha and gamma tubulins); fixed cells were permeabilized with Triton^{TM} X-100 (Sigma #T8787) 0.05% for 15′ at RT, and blocked for 1 h with 10% goat serum (Gibco #16210-072); primary antibodies were incubated overnight at 4°C (anti-alpha tubulin Sigma #T9026; anti-gamma tubulin Sigma #T3559; anti-R-loops S9.6 Merk #MAB1095; anti-HP1 Santa Cruz #sc-515341; anti-H3K9me3 #ab176916); slides were washed 3X with PBS and incubated 1 h at RT with the appropriate Alexa Fluor secondary antibody (Thermo Fisher) and DAPI (Sigma Aldrich) to counterstain the nuclei; after 3X PBS washes slides were mounted with ProLong^{TM} Gold Antifade mounting solution (Thermo #P36934) and acquired in z stack mode with confocal laser microscope (NIKON Eclipse Ti) using EZ C.1 acquisition software (Nikon, Tokyo, Japan); all the images were processed using FIJI software (ImageJ). The fluorescent intensity profiles of HP1 and H3K9me3 were performed with NIS elements analysis software 6.0 (Nikon). Micronuclei analysis has been made with NIS elements software (Nikon) and for each field (6–15 random field/sample) the number of micronuclei (counted using a threshold of 0.2-2μM) were divided by the number of nuclei (counted using a threshold size 5–20μM). R-loops analysis has been performed by calculating the percentage of R-loops positive cells per field (6–12 random field/samples; clear and strong S9.6 signal). The polar microtubules (alpha tubulin) and the centrosome (gamma tubulin) has been used to count the number of mitotic poles per cell. The nuclear size was determined by using FIJI software and the data are represented as dC-treated/not-treated (dC/nt).

DNA fibre assay

The DNA fibre assay was performed as described in (Quinet et al., 2017). Cells were treated with IdU (20μM; Sigma #I7125) for 30′, washed 3 times with PBS, then treated with CldU (200μM; Sigma #C6891) for 30'. After DNA labeling, cells were resuspended in PBS (1000–2000 cells/μL) and 2μL drop containing cells was transferred to a positively charged glass slide and lysed with 8μL lysis buffer (200 mM Tris-HCl pH 7.5; 50 mM EDTA; 0.5% SDS); the slide was tilted at 30–45° to allow the DNA to spread slowly down the slide; the DNA fibres were fixed with methanol:acetic acid (3:1) for 5′ and washed 2X with PBS; the DNA was denatured with HCl 2.5 M at RT for 1 h, washed 3X with PBS and blocked 1 h with PBS-BSA 5%; slides were incubated with mouse anti-BrdU (BD, #347580, to label IdU) and rat anti-BrdU (Abcam, #Ab6326, to label CldU) in PBS-T-BSA (Tween 0.1%, BSA 5%) 3 h at RT, washed 3X with PBS, then incubated with secondary antibody (anti-mouse Alexa Fluor 547 #A21123; anti-rat Alexa Fluor 488 #A21470) in PBS-T-BSA 1 h at RT; finally, after 3X washes in PBS slides were mounted with ProLong^{TM} Gold Antifade mounting solution (Thermo #P36934) and acquired as described before; the fibre length (100–200 fibres per samples) was measured in μm with FIJI (ImageJ), then converted in Kilobases by applying the conversion factor of 2.59 Kb/μm; the replication fork velocity (Kb/min) was calculated by dividing the fibre length by the nucleoside analogues incubation timing.

Proximity ligation assay (PLA)

Cells were fixed with PFA 4% in PBS, permeabilized as described before and incubated with primary antibodies (anti-PCNA Santa Cruz #sc-56; anti-γH2AX Merk #05-636). For labelling and PLA signal amplification, the Duolink^{TM} In Situ Red Mouse/Rabbit kit (Sigma) was used according to the manufacturer's protocol. Images were acquired in Z-stack mode as described before and 150–200 nuclei per sample were analyzed using FIJI software (ImageJ) to count the PLA spots per nucleus.

Dot blot

R-loops analysis by Dot blot has been performed as described in Ramirez et al., 2021 (jove protocol 62069; https://doi.org/10.3791/62069). The cells were collected by using trypsin, and the cell pellet were lysed with cell lysis buffer (10% NP-40, 2 M KCl, 0.5 M PIPES ph 8.0) to obtain a nuclear pellet. The nuclear pellet was lysed with nuclear lysis buffer (10% SDS, 1 M Tris-HCl ph 8.0, 0.5 M EDTA) and treated with 200 μg/mL proteinase K for 3 h at 55°C. Genomic DNA was purified following two consecutive extraction steps using 1 volume of phenol:chloroform:isoamyl alcohol (25:24:1 pH 8.0) first, and 1 volume of chloroform later. The DNA was then precipitated by 0.3 M sodium acetate, glycogen, and ice-cold 100% ethanol; the DNA pellet was then washed with 70% ethanol and the air-dried pellet resuspended in elution buffer (1 M Tris-HCl ph 8.0). The purified DNA was treated or not treated (mock) with RNase H (New England Biolabs, #M0297L) 15 min at 37°C; 2-4μL of samples were then loaded on a positively nylon membrane subsequently crosslinked with UV light (1.200μJ x 100). The membrane was blocked with 5% milk in PBS with 0.05% Tween-20 for 1 h at room temperature, and then incubated with 1μg/mL S9.6 antibody in blocking solution 2 h at room temperature; after 3 washes in PBS-Tween the membrane was incubated with peroxidase-conjugated secondary antibodies (Bio-Rad) at room temperature for 1 h; detection was performed with the ECL chemiluminescence kit (Perkin Elmer). After S9.6 signal detection, the membrane was washed twice and stained with methylene blue for 30 min at room temperature to detect total genomic DNA. The S9.6 and methylene blue signal were quantified using ImageJ; the values from S9.6 analysis were then normalized on methylene blue signal values (S9.6/methylene blue).

Gene Ontology (GO) term enrichment analysis

Gene ontology analysis has been performed by launching the 4097 genes (differentially modulated between shCTR and shp53 from RNAseq experiment) in the *Mus musculus* biological process windows on geneontology.org web site. The selected categories from

PANTHER Overrepresentation test (https://doi.org/10.5281/zenodo.6399963) are graph based on Fold Enrichment and they all have a FDR p-value<0.05; Fisher's Exact test corrected by False Discovery Rate was used.

Western blot

Cells were lysed with RIPA buffer, and the samples were denatured at 98°C, resolved on a SDS–polyacrylamide gel, and blotted on Amersham Hybond P0.45 PVDF membrane (GE Healthcare Life Science); membranes were blocked by Blotting-Grade Blocker (Bio-Rad) 5% in PBS 0.1% Tween-20, incubated with primary antibodies overnight at 4°C (anti-p53 Santa Cruz #sc-126; anti-Gapdh, anti-β-actin Sigma, anti-H3, and anti-H3 lysine methylations listed in key sources table) washed 3X with PBS 0.1% Tween-20, and incubated with the appropriate peroxidase-conjugated secondary antibodies (Bio-Rad) at room temperature for 1 h; detection was performed with the ECL chemiluminescence kit (Perkin Elmer).

Intracellular SAM measurement

Cells were collected, resuspended with cold PBS, and lysed by sonication (Bioruptor^{TM} UCD-200 Diagenode, high voltage, 30"ON - 30"OFF for 5′ at 4°C). The SAM concentration in the supernatant was measured by Mouse S-Adenosylmethionine (SAM) ELISA Kit (MyBioSource, #MBS2603023) following the manufacturer's instruction.

RT-qPCR

Total RNA was extracted with RNeasy Mini Kit (QIAGEN, #74106). A second DNase step (the first during the RNA extraction procedure) was performed using DNaseI (Sigma, #AMPD1-1KT), and 500 ng of RNA were retrotranscribed by SensiFAST^{TM} cDNA Synthesis Kit (Bioline, #BIO.65054) according to the manufacturer's protocols. qPCR was performed using Fast SYBR^{TM} Green Master Mix (Thermo, #4385612). The primers used are listed in key resources table. The expression of each gene was defined from the threshold cycle (Ct), and the relative expression levels were calculated by using the $2^{-\Delta\Delta Ct}$ method after normalization with reference to expression of housekeeping gene.

RNA fluorescent in situ hybridization (RNA FISH)

Custom Stellaris® FISH Probes were designed against Major Satellite (Biosearch Technologies, #SMF-1063-5) using a 788 bp array at murine chromosome 2 as template (Chr2:98.506.702-98.507.489; UCSC mm9; (Kishikawa et al., 2016; Ting et al., 2011). Cells were fixed in methanol (10′) and acetone (1′) on ice, then permeabilized in 70% Ethanol for 15′ at 4°C. The fixed cells were hybridized with the probe labelled with Quasar 570 dye (Biosearch Technologies, Inc.), following the manufacturer's instructions available online at www.biosearchtech.com/stellarisprotocols. For the double staining (Maj Sat FISH and R-loops IF), the primary antibody (S9.6, Millipore) was added together with the FISH probe during the hybridization step (4 h at 37°C); secondary antibody and DAPI were added during the two following wash steps (30′ each at 37°C). The images were acquired as described before.

Chromatin immunoprecipitation (ChIP)

Cells were fixed with 1% formaldehyde for 10 min and the reaction was quenched with 0.125 M glycine; chromatin fragments (300–600 bp) were obtained by sonication (Bioruptor^{TM} UCD-200 Diagenode, high voltage, 30"ON - 30"OFF for 25′ at 4°C); the immunoprecipitation was conducted using Dynabeads Protein G (Invitrogen, #10004D), followed by reverse cross-link with Proteinase K (20 mg/mL, Thermo) and 0.1 mg/mL RNase A (Thermo); the DNA was purified by QIAquick PCR kit (QIAGEN) and the major satellite regions, Mdm2 and Gapdh promoters, and Slc43a2 intron were amplified by real-time qPCR (primers in key resources table). The following antibodies were used: anti-p53 (Leica, cat. P53-CM5P-L), anti-H3K9me3 (Abcam, #ab176916), anti-H3K9me1 (Abcam, #ab176880) and mouse/rabbit IgG Isotype as control (Invitrogen).

Metaphase chromosomes preparation

Cells were treated with colchicine (5 μg/mL) for 24 h before collection; cell pellet was incubated with hypotonic buffer (12.3 mM HEPES ph 7.5; 0.53 mM EGTA; 64.4 mM KCl) 30′ at 37°C and fixed with methanol:acetic acid (3:1) 10′ at RT; after 4 washes with fixative solution, 10μL of cells suspension (~8000 cells) was dropped onto a glass slide from an high of ~5 cm; slides were dried, stained with DAPI and acquired as described before.

SAM supplementation

The day after plating, the cell medium was supplemented with 200μM SAM (Sigma, #A7007) 24 h before dC treatment, until the sample collection. Maj Sat RNA and micronuclei count were performed as described above.

ATAC-seq (assay for transposase-accessible chromatin using sequencing)

The cell pellet (KPCshp53 ± doxy 48 h dC-treated; 2 biological replicates) was resuspended in 500μL of ice-cold cryopreservation solution (50% FBS, 40% growth media, 10% DMSO); Active Motif performed the ATACseq. The paired-end 42 bp sequencing reads (PE42) generated by Illumina sequencing NextSeq 500 are mapped to the mouse genome (mm10) using the BWA algorithm with default settings. Alignment information for each read is stored in the BAM format. Only reads that pass Illumina's purity filter, (no more than 2 mismatches) and map uniquely to the genome are used in the subsequent analysis. Duplicate reads removed. Genomic

regions with high levels of transposition/tagging events are determined using the MACS2 peak calling algorithm (Zhang et al., 2008). Both reads from paired-end sequencing are used for peak-calling but treated a single, independent reads. To identify density of transposition events, the genome is divided into 32 bp bins and the number of fragments in each bin is determined. Reads are extended to 200 bp, which is close to the average length of the sequenced library inserts. The "signal map" is stored in a bigWig file, which can be visualized in genome browsers. In the default analysis, the tag number of all samples is reduced (by random sampling) to the number of tags present in the smallest sample. To compare peak metrics between 2 or more samples, overlapping intervals are grouped into "Merged Regions", which are defined by the start coordinate of the most upstream interval and the end coordinate of the most downstream interval. After identifying merged regions, the DESeq2 software is run on the unnormalized BAM files. The program then normalizes the counts between the samples using the "median of ratios" method, and calculates log2 fold-change (Log2FC), shrunken-Log2FC, p-value, and adjusted p-value (padj, FDR) for each Merged Region corrected for multiple testing. Visualization of ATAC-seq tracks of the Major Satellite genomic regions were obtained by using the IGB software. The peaks signal amplitude has been calculated using ImageJ.

RNA-seq
Total RNA from 3 biological replicates (KPCshp53 ± doxy 48 h dC-treated; 2 biological replicates) was extracted as described before (RNeasy Mini Kit QIAGEN, #74106; DNaseI Sigma, #AMPD1-1KT); Active Motif performed sequencing and bioinformatic analysis. Briefly, the paired-end 42 bp sequencing reads (PE42) were generated and mapped as described above. The number of fragments overlapping predefined genomic features of interest and only read pairs that have both ends aligned, are counted. Read pairs that have their two ends mapping to different chromosomes or mapping to same chromosome but on different strands are discarded. The gene annotations come from NCBI RefSeq database and then adapted by merging overlapping exons from the same gene to form a set of disjoint exons for each gene. Genes with the same Entrez gene identifiers were also merged into one gene. After obtaining the gene table containing the fragment counts of genes, we perform differential analyses to identify statistically significant differential genes using DESeq2. The DESeq2 model internally corrects for library size using their median-of-ratios method. The gene table obtained is used as input to perform the DESeq2's differential test. After a differential test, the p-value of each gene is calculated and adjusted to control the number of false positives among all discoveries at a proper level (multiple testing adjustment). The DESeq2 by default filters out statistical tests (i.e. genes) that have low counts by independent filtering technique. All genes with average normalized counts below a filtering threshold from multiple testing adjustment are omitted. Differential genes are detected by DESeq2 at 0.1 (or 10%) FDR (i.e. adjusted p-value).

Live cell imaging
Cells were seeded in 35-mm high glass bottom dishes for cell culture (Ibidi) and transfected with the plasmids FLAG-MaSat-NLS-ZF-18-mVenusN, FLAG-mVenusC-14-HP1b-Chromo in a 1:5 ratio (Lungu et al., 2017) and DUAL-tandem-Tomato (Addgene) using Lipofectamine^{TM} 3000 Transfection Reagent (Thermo, #L3000015) following the manufacturer's instructions; 24 h after transfection the cells were treated with 10μM of dC and placed in the incubator chamber for live cell imaging (LAUDA E200 with CO_2 controller DGTCO2BX okolab). Time-lapse images were acquired with confocal laser microscope (NIKON Eclipse Ti) using EZ C.1 software (Nikon, Tokyo, Japan) at 30 min of interval and Z-stacks acquired every 0.4μM; videos were processed by NIS element analysis software 6.0 and FIJI (ImageJ).

Bisulfite conversion reaction
The cells were treated with 10μM dC for 48 h. Genomic DNA was extracted with Wizard Genomic DNA purification kit (Promega #A1125) and 1 μg was used for the Bisulfite Conversion kit (Active Motif, #55016) following manufacturer's guidelines. The converted DNA was analyzed by endpoint PCR using Xpert Fast Hotstart Mastermix (Grisp, #GE45.5001). Primers able to recognize the different methylation status of Major Satellite were designed with MethPrimer website (https://www.urogene.org/methprimer/, Li and Dahiya, 2002; key resources table) by using a 788 bp Maj Sat array as template (Chr2:98.506.702-98.507.489; UCSC mm9;). PCR products were analyzed by electrophoresis on 2% agarose gel.

Slc43a2 cloning
Slc43a2 was amplified by RT-PCR using RNA from KPshCTR cells (-doxy, p53 wt) and the primers listed in key resources table; the obtained product was purified using QIAquick PCR Purification Kit (QIAGEN, #28104), digested with NheI (New England Biolabs, #R3131) and HindIII (New England Biolabs, #R0104L) 2 h at 37°C to obtain sticky ends, then purified again. The Slc43a2 insert were then cloned into pcDNA3.1 (containing ampicillin resistance and digested as describe above) by ligation (1:3 ratio vector:insert) using Quick ligase (New England Biolabs, #M2200L) for 1 h at room temperature; the ligation product was used to transform One Shot^{TM} TOP10 Chemically Competent *E. coli* (Thermo Fisher #C404010) and a single selected clone (by ampicillin resistance) containing the Slc43a2 expressing vector was used for subsequent bacterial amplification and plasmid purification.

Bioinformatical analysis of PDAC datasets
Publicly available datasets were used to compute correlations analyses of metabolomic (Daemen et al., 2015), transcriptomic and proteomic (Cao et al., 2021), genomic (cBioPortal), and survival (cBioPortal) data of PDAC patients and cell lines; they are all listed

in the key resources table and mentioned in figure legend and/or main text. ChIP-seq analysis in Figure 5I was carried out using the bigwig file SRX2170272 downloaded from https://chip-atlas.org/. The ChIP-seq tracks were extracted using IGB software.

QUANTIFICATION AND STATISTICAL ANALYSIS

GraphPad Prism was used for all test calculations and all data are expressed as mean ± standard error (SEM), unless otherwise mentioned. One-way ANOVA, two-tailed tests (e.g. student's t-test, Mann-Whitney test), X2 (chi square) were used to calculate the p-value, unless otherwise mentioned; a p-value lower than 0.05 was selected to state statistically significant differences. More details on quantification and statistical tests used in this study are specifically indicated in figure legends and methods.